A New Complete Sample of Sub-millijansky Radio Sources: An Optical and Near-Infrared Study

Frank J. Masci[1,2], J. J. Condon[3], T. A. Barlow[1], C. J. Lonsdale[1], C. Xu[1], D. L. Shupe[1], O. Pevunova[1,4], F. Fang[1] and R. Cutri[1]

Received _____; accepted _____

[1]Infrared Processing and Analysis Center, M/S 100-22, California Institute of Technology, Jet Propulsion Laboratory, Pasadena, CA 91125

[2]Electronic mail: fmasci@ipac.caltech.edu.au

[3]National Radio Astronomy Observatory, 520 Edgemont Road, Charlottesville, VA 22903

[4]Present address: Interferometry Science Group, M/S 171-122C, Jet Propulsion Laboratory, Pasadena, CA 91109-8099

ABSTRACT

The Very Large Array (VLA) has been used in C-configuration to map an area $\simeq 0.3\,\mathrm{deg}^2$ at 1.4 GHz with 5σ sensitivities of 0.305, 0.325, 0.380 and 0.450 mJy beam^{-1} over four equal subareas. Radio properties are presented for 62 detected sources. Deep optical imaging to Gunn $r \simeq 25$ mag using the Hale 5-m telescope covering $\simeq 0.21\,\mathrm{deg}^2$ is reported for a subset of 43 sources. This optical follow-up is much deeper than that of existing larger area radio surveys of similar radio sensitivity. Archival J, H and K-band photometry from the Two-Micron All Sky Survey (2MASS) is also presented. Using a robust likelihood-ratio technique, we optically identified 26 radio sources with probabilities $\gtrsim 80\%$, nine are uncertain/ambiguous detections, and eight are empty fields. Comparisons with a stellar synthesis model that includes radio emission and dust reddening suggests that the near-infrared–to–optical emission in a small, bright sub-sample is reddened by 'optically thin' dust with absorption $A_V \simeq 2 - 2.5$ mag, regardless of morphological type. This is consistent with other, more direct determinations of absorption. The radio–to–optical(–near-infrared) flux ratios of early-type galaxies require significant contamination in the radio by an active galactic nucleus (AGN), consistent with the current paradigm. Using our simple modeling approach, we also discuss a potential diagnostic for selecting Ultraluminous Infrared Galaxies (ULIGS) to $z \simeq 1.6$ from microJansky radio surveys.

Subject headings: galaxies: active — galaxies: starburst — cosmology: observations — radio continuum: galaxies

1. INTRODUCTION

The advent of deep radio surveys reaching flux densities well below 1 mJy (Mitchell & Condon 1985; Windhorst et al. 1985; Oort 1987; Windhorst et al. 1993; Hopkins et al. 1998; Richards 2000) revealed a new population of faint sources more numerous than the AGN-powered radio galaxies dominating the strong-source population. This corresponds to a steepening of the differential source counts over non-evolving predictions at levels $\lesssim 4$ mJy. The faint counts suggest that significant evolution has occured over the redshift range spanned by the observed population. Photometric and spectroscopic studies (Thuan et al. 1984; Windhorst et al. 1985; Thuan & Condon 1987; Benn et al. 1993) suggest that the faint excess at 1.4 GHz is composed predominately of star-forming galaxies similar to the nearby starburst population dominating the *Infrared Astronomical Satellite* (*IRAS*) 60-μm counts (Benn et al. 1993). Indeed, this is supported by the strong correlation between radio (1.4 GHz) and far-infrared (60-μm) flux densities of disk galaxies (Helou, Soifer & Rowan-Robinson 1985), implying a significant proportion of starburst galaxies at faint radio flux densities.

The overall observed source-count distribution from faint (μJy) to bright ($S_{1.4} \gtrsim 10$mJy) flux densities cannot be explained by starbursts alone. Evolutionary models of radio source counts need to invoke two separate populations (eg. Danese et al. 1987; Rowan-Robinson et al. 1993; Hopkins et al. 1998). Condon (1989) describes these populations as starbursts and monsters, each powered by different mechanisms: 'starbursts' deriving their radio emission from supernova remnants and HII regions and 'monsters' from compact nuclear related activity (eg. active galactic nuclei; AGNs). The proportion of AGN is much greater at higher flux densities $S_{1.4} \gtrsim 10$ mJy (Kron, Koo & Windhorst 1985; Gruppioni et al. 1998), where a majority are associated with classical radio galaxies exhibiting extended (FRI and FRII-type) morphologies (Fanaroff & Riley 1974). The optical counterparts to

sources at bright radio flux densities $S_{1.4} \gtrsim 1$ mJy is comprised mostly of ellipticals while at sub-mJy to μJy levels, the optical counterparts are identified as blue galaxies exhibiting peculiar (compact, interacting and irregular) morphologies (Kron, Koo & Windhorst 1985; Gruppioni et al. 1998). Studies of faint radio sources, namely their stellar population, how they evolve with redshift, and how they relate to local normal galaxies is progressing rapidly, however, much remains to be learned from the faintest (μJy) radio populations at redshifts $1 \lesssim z \lesssim 2$.

Radio surveys are insensitive to the effects of absorption by dust which is known to bias surveys severely at optical/UV wavelengths. This is particularly important for derivations of the cosmic history of star formation and its relation to hierarchical models of galaxy formation. Optical/UV studies have shown that there is an increase in both the space density of star-forming, morphologically disturbed galaxies (eg. Richards et al. 1999) and also, the global star formation rate with redshift to $z \gtrsim 1$ (eg. Madau et al. 1996). Similar evidence is emerging from studies of sub-mm sources (Blain et al. 1999) and amongst the faint radio population at $1 \lesssim z \lesssim 2$ - the redshift range probed by the deepest surveys (eg. Cram 1998; Haarsma et al. 1999).

There has been much speculation as to whether global star-formation rates (SFRs) derived from radio observations exceed those determined from optical/UV studies. Cram et al. (1998) note that systematic discrepancies may exist between the various star formation indicators, which are not well understood (see also Schaerer 1999). It is encouraging to see however that Haarsma et al. (2000) find global SFRs derived from 1.4GHz observations of the Hubble Deep Field to exceed optically detetermined values by a factor of a few out to $z \sim 1$. Indeed, an analysis of Balmer decrements and optical–near-infrared colors in star forming galaxies by Georgakakis et al. (1999) from the Phoenix Deep Survey (Hopkins et al. 1998), finds evidence for visual extinctions from one to a few magnitudes. Currently,

about 20% of existing micro-jansky radio samples remain unidentified to $I = 25$ mag in Hubble Deep Field images (eg. Richards et al. 1999). A majority of these could represent a significant population of dust-enshrouded starbursts and/or AGN at high redshift. These results are in support of efforts to further understand the dust properties of star-forming galaxies.

The primary aim of this paper is to introduce a new complete sample of radio sources selected at 1.4 GHz, uniformly selected over the flux range $S \gtrsim 0.3$ mJy (5σ) from an area covering $\simeq 0.3\,\mathrm{deg}^2$. Although much larger area surveys to deeper radio sensitivities have been carried out (eg. Hopkins et al. 1998), the present study reports the results of more sensitive optical observations. Archival near-infrared data for a subset of the sample are also presented. The near-infrared data is from the ongoing 2MASS project, and represents a unique aspect of this study in the identification of radio-selected starbursts. Although we currently lack valuable spectroscopic information, we combine radio–near-infrared–optical flux ratios, radio maps, and optical images to explore the properties of the entire sample. Our deep optical identifications provide the opportunity to asses the importance of dust in star-forming systems via the observed radio–to–optical and near-infrared–to–optical colors. Simple stellar synthesis models that include radio emission and reddening are used to constrain possible amounts of absorption.

This paper is organised as follows. In §2, we discuss the radio observations and data reduction, present the radio catalog, and compare our results with data available from (shallower) all sky radio surveys. The optical photometric observations, their reduction and astrometric calibrations are discussed in §3. Our method for radio-optical identification, the archival near-infrared data, radio-optical image overlays, and our optical/near-infrared catalog are presented in §4. A study of the radio, near-infrared, and optical colors and constraints on synthesis models incorporating dust is presented in §5. An application of our

color-color analysis to select high-redshift ultraluminous infrared galaxies from deep radio surveys is discussed in §6. All results and future prospects are summarised in §7.

2. RADIO OBSERVATIONS

2.1. Strategy

Observations were made with the VLA C-configuration at 1.4 GHz on 1998 December 19. This configuration yields a good compromise for resolution and surface-brigntness sensitivity. The 5σ confusion limit for this configuration is only 50μJy/beam at 1.4 GHz (Mitchell & Condon 1985) since the synthesised beam size (Full Width at Half Power; FWHP) is ~ 15 arcsec. The resulting radio positions have rms errors ~ 1 arcsec, except for extended sources with multiple components, sufficient for making optical identifications. At 1.4 GHz the FWHP of the VLA primary beam is 31 arcmin and approximately corresponds to the diameter of our final imaged field. This relatively large coverage avoids field-to-field variations in source counts induced by high-redshift clustering. Although surveys at higher frequencies (eg. 8 GHz) can reach lower flux densities than at 1.4 GHz, most radio sources have spectral indices $\alpha \sim 1$ ($S \propto \nu^{-\alpha}$) so that the population being sampled is similar.

To provide uniform sensitivity over the full area of our field, we observed seven positions arranged in a filled hexagonal pattern with a separation of $26'$ between pointing centers. The resulting root mean square (rms) map noise is thus nearly constant (cf. Condon et al. 1998). Our field was centered on RA(2000)=$00^h13^m12^s.0$, Dec.(2000)=$+25°54'44''$. This field was chosen for its relatively low foreground galactic-cirrus emission likely to affect optical/near-infrared identifications and also for the absence of bright radio galaxies. The integration time on each pointing was ~ 1 hour. This allowed us to reach an rms noise of $\sim 60\mu$Jy in regions free from bright contaminating sources (see § 2.3 for more details).

Our observations were made in spectral line mode with four Intermediate Frequencies (IFs), each divided into 7 spectral channels of width 3.125 MHz. The advantage of this mode is to minimize bandwidth smearing (i.e. chromatic aberration) which reduces the point-source sensitivity away from the pointing center and causes appreciable image distortion. Additionally, the spectral line mode is less prone to narrowband interference noise spikes. With continuum mode however, we would have had a little over twice the bandwidth and a factor $\approx \sqrt{2}$ lower noise.

2.2. Data Reduction

The data were analysed with the NRAO `AIPS` reduction package. We observed 3C 48 to calibrate the visibility amplitudes, using $S = 16.5$ and $S = 15.9$ Jy at 1.365 and 1.435 GHz, respectively. The calibration was applied using the `SPLIT` task. The calibrated data from each pointing were edited and imaged separately, `CLEAN`ed, and restored with 15 arcsec FWHP Gaussian beams. The seven separate images were weighted and combined as described in Condon et al. (1998) to produce a final $33' \times 33'$ map with nearly uniform sensitivity and corrected for primary-beam attenuation.

2.3. Noise and Source Extractions

The resulting rms noise of our final map after correcting for primary-beam attenuation is not uniform over the entire field, but increases by up to 30% near a strong ($\gtrsim 400$ mJy) source near the edge of our field. Despite this variation in sensitivity, we were able to divide our $33 \times 33\,\mathrm{arcmin}^2$ field into four equal ($\approx 16.5 \times 16.5\,\mathrm{arcmin}^2$) regions within which the rms noise varies by no more than a few percent. These constant-noise regions simplify the application of an automated source-finding algorithm over a single continuous region (see

below). The lowest and highest rms noise amongst these regions was $\simeq 60.9\,\mu$Jy/beam and $\simeq 90.3\,\mu$Jy/beam respectively. See Table 1 for the region definitions. The rms noise of each region was estimated from the Gaussian core of the amplitude distribution of the pixel values as produced by the `AIPS` task `IMEAN`. In Figure 1, we show the distribution in pixel values of our entire $33'$ field. The rms deviation in peak flux density derived from a fit to this histogram is $\simeq 69\mu$Jy/beam. Figure 2 shows a contour map of our entire radio field.

Each constant-noise region in Table 1 was used for the source extractions. Within each region, we searched for radio sources down to a peak flux density ≥ 5 times the rms value of the region. The sources were extracted by the AIPS task `SAD` which uses Gaussian fits to estimate the fluxes, positions, and angular sizes of the selected sources. For faint sources however, unconstrained Gaussian fits may be unreliable (see Condon 1997). For this reason, we adopted the following method for the source extraction: first, we ran the task `SAD` with a $3\sigma_{rms}$ detection threshold to obtain an initial list of candidates, we then derived the peak flux densities of the faint sources (with $3\sigma < S_{peak} < 7\sigma$) using the `MAXFIT` task. This task uses a second order interpolation algorithm and is known to be more accurate. Only sources with a `MAXFIT` peak flux density $\geq 5\sigma_{rms}$ were retained. For these faint sources, the total flux density was estimated using the task `IMEAN`, which integrates the (median background subtracted) pixel values in a specific rectangle. The rectangle was chosen to encompass as much of the source as possible. For all other parameters (sizes, positions and position angles) we retained the values obtained from the initial Gaussian fits. Only two sources had irregular morphologies showing multiple components. For these, the total (background subtracted) flux was determined using the task `TVSTAT` which allows an integration over a specific irregular area defined to encompass as much of the source as possible.

The numbers of sources detected in each constant-noise region are summarised in Table 1. A total of 62 sources were detected with flux densities $\geq 5\sigma_{rms}$ over an area of

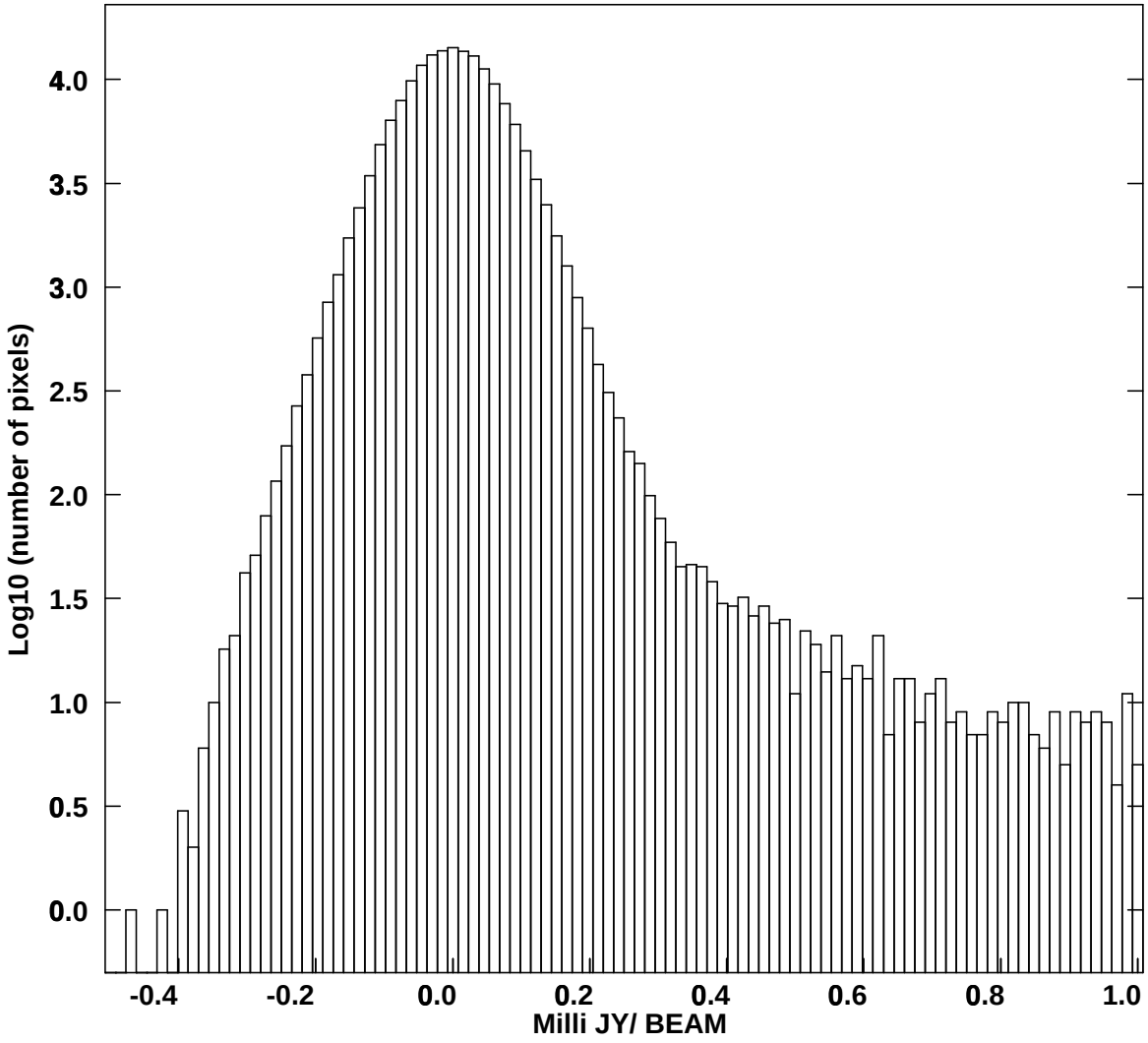

Fig. 1.— Logarithmic histogram of pixel flux densities in our complete radio map.

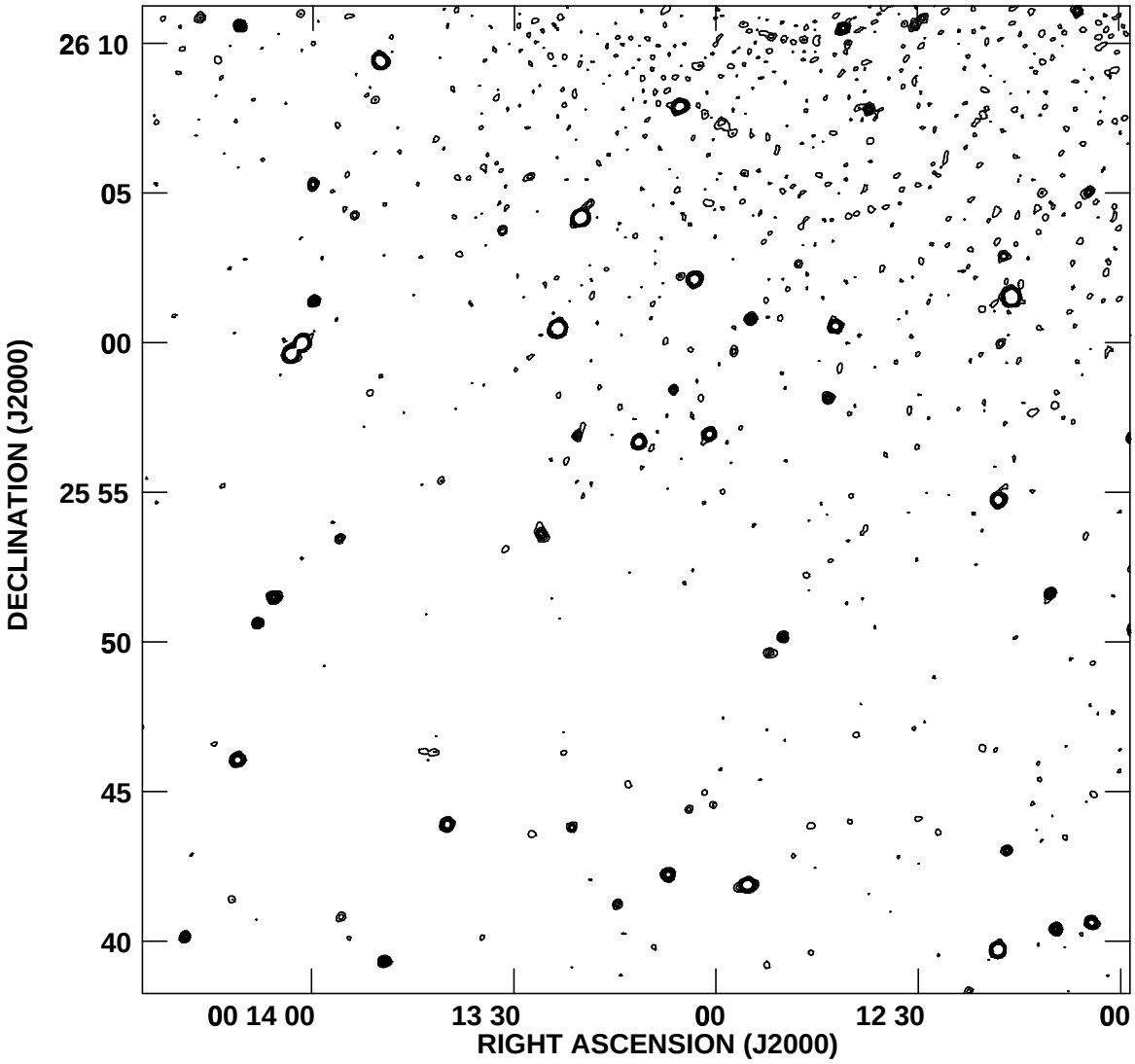

Fig. 2.— Contour plot of our radio map covering an area $33 \times 33\,\mathrm{arcmin}^2 = 495 \times 495$ pixels. Contour levels are 0.2, 0.4, 0.6, 0.8, 1.0, 1.2, 1.4, 1.6 mJy/beam. Note the increase in rms noise from the bright off-field source in the top right corner.

$0.303\,\mathrm{deg}^2$. Within poisson uncertainties, this number is consistent with source counts from surveys by Ciliegi et al. (1999) and Hopkins et al. (1998). To our limiting (mean) sensitivity of 0.35mJy and within $0.303\,\mathrm{deg}^2$, they report a source count of typically 70 ± 8. This confirms the reliability of our radio source detections and flux density estimates.

Table 2 shows the full radio catalog which reports (in column order): the source name; RA and Dec.(J2000); errors in RA and Dec.; the peak flux density S_P; error in S_P; the total flux density S_T; error in S_T; the full width half maximum (FWHM) of the major and minor axes θ_M and θ_m (determined from Gaussian fits); the position angle PA of the major axis (in degrees); and the rms errors associated with θ_M, θ_m, and PA respectively. The different components of multiple sources are labelled "C1" and "C2". In Figure 3, we show the distribution of peak flux densities and the total to peak flux ratio as a function of peak flux for all sources. Sources with ratios $S_T/S_P < 1$ in Figure 3b are primarily due to uncertainties on measured fluxes as estimated from the two dimensional Gaussian fits. Uncertainties in peak fluxes are typically $\lesssim 10\%$, while total flux estimates are more uncertain due to a sensitive dependence on the Gaussian fitting procedure. Errors in total fluxes are typically $\lesssim 30\%$. Contour maps of radio sources with available optical data are shown in Figure 8.

2.4. Comparison with the *NVSS* Catalog

The $33 \times 33\,\mathrm{arcmin}^2$ region that we observed with the VLA was also covered by the NRAO VLA Sky Survey (Condon et al. 1998, NVSS). The NVSS covers the sky north of $\delta = -40°$ at 1.4 GHz with $45''$ resolution and limiting flux density of $\simeq 2.25$ mJy (5σ). To this limit, 17 of our sources were found to be in common with the NVSS public catalog. One source in our catalog however is a double component source and is unresolved by the NVSS. A comparison of flux densities derived in this study with those from this catalog

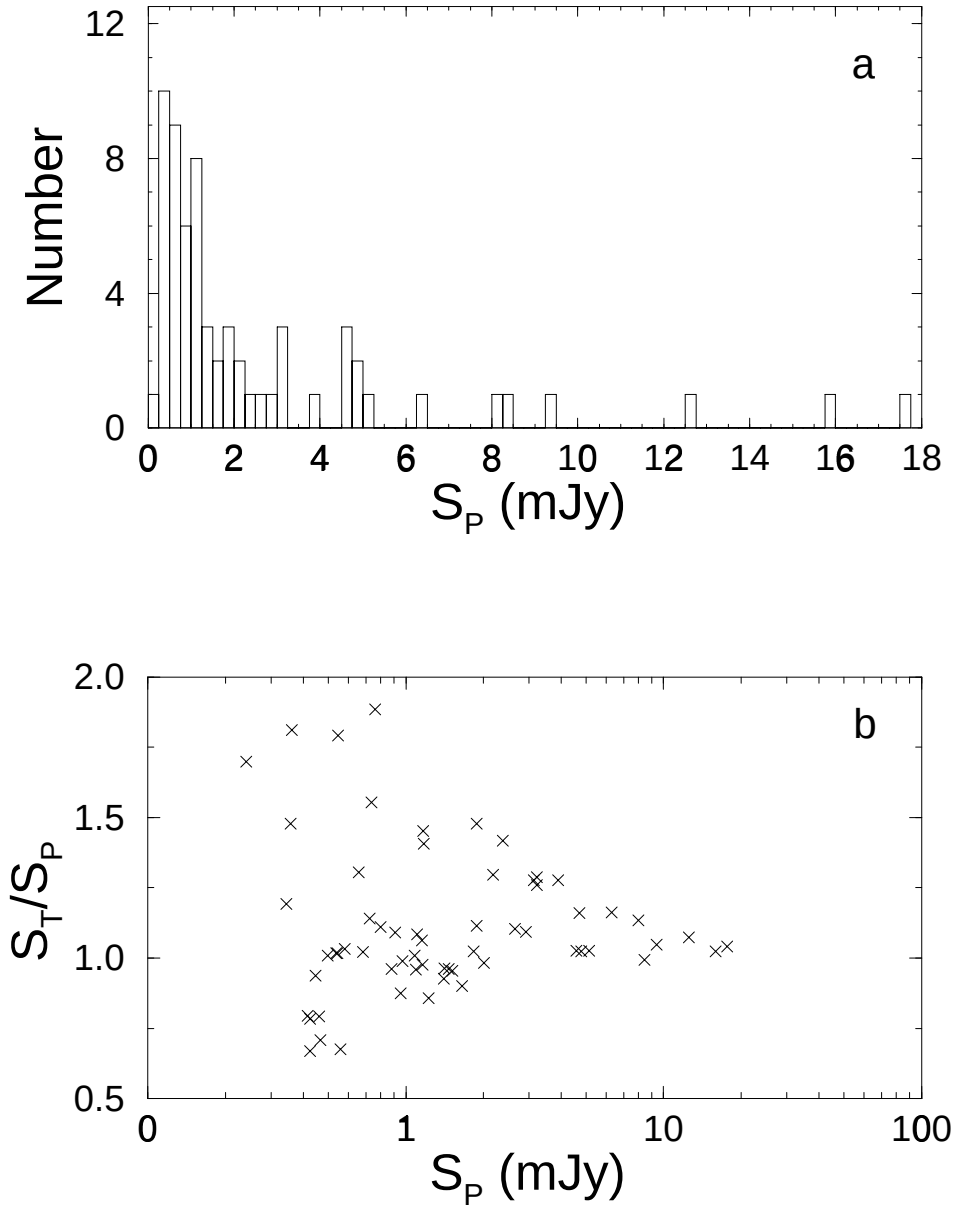

Fig. 3.— (a) Distribution of peak flux density and (b) total to peak flux ratio as a function of peak flux.

is shown in Figure 4. It is evident that our derived flux densities are on average slightly lower than those from the NVSS. This was also reported in a larger comparison study by Ciliegi et al. (1999) using a similar observational set-up and can be explained by the difference in resolutions used in the two surveys: $15''$ vs. $45''$. High-resolution surveys tend to miss flux from low-surface-brightness emission. Although the effect is only marginal for bright sources, it may become important for attempts to detect faint, low-surface-brightness objects at high redshift.

3. OPTICAL PHOTOMETRIC OBSERVATIONS

3.1. Observations and Data Reduction

Optical CCD photometry of our radio field was carried out on the 5-m Hale telescope at Palomar[5] Observatory during the nights of 27-29 August 1997. These fields were initially selected for subsequent deep mid-IR imaging with the *Wide Field Infrared Explorer* mission (*WIRE*), but the mission failed to perform to expectations. The Carnegie Observatories Spectroscopic Multislit and Imaging Camera (COSMIC; Kells et al. 1998) mounted at the $f/3.5$ prime focus with a TEK 2K CCD was used to image nine $9.7 \times 9.7\,\mathrm{arcmin}^2$ fields in the Gunn r (6550Å) filter. Each optical field comprised of three optical pointings offset by $2'$, each with integrations of 600 sec giving a total 1800 sec per field. This resulted in a limiting magnitude of $r \simeq 25$ mag (5σ). The seeing was typically $1 - 1.4''$ (FWHM). The optical fields do not cover our entire $33 \times 33\,\mathrm{arcmin}^2$ radio field. The nine slightly overlapping optical fields correspond to an areal coverage $27.5 \times 27.5\,\mathrm{arcmin}^2$, or about 70% of the radio map.

[5]Operated by California Institute of Technology, Pasadena, CA 91125

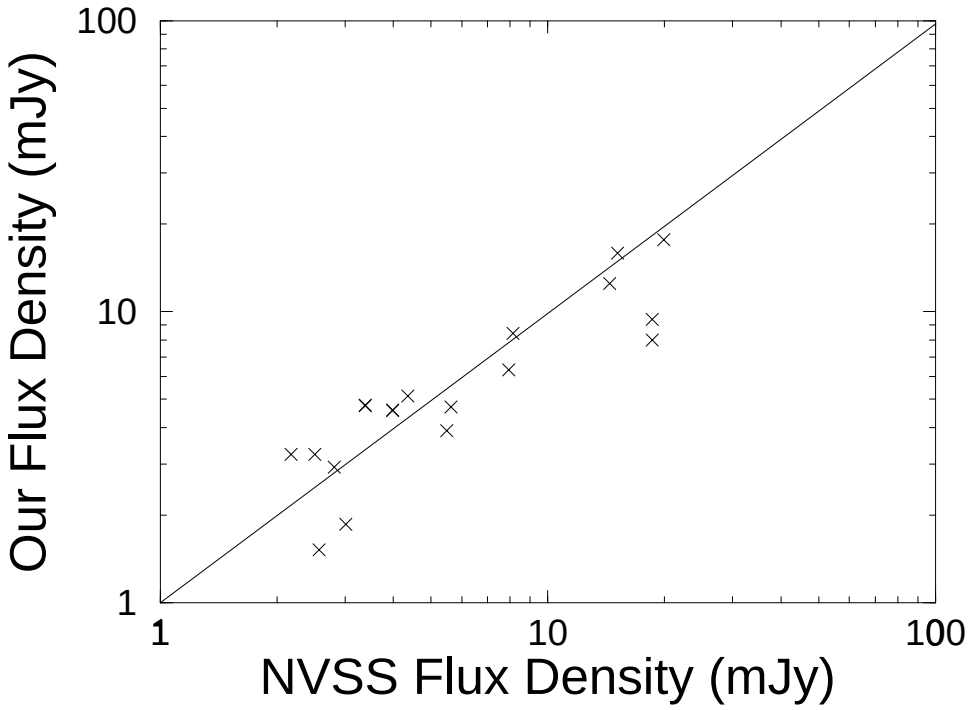

Fig. 4.— The peak flux density obtained with our survey versus that reported for the same sources in the *NVSS* public database.

The CCD data were reduced with standard tasks in the IRAF package. Frames were first bias-subtracted, then flat-fielded using dome flats. Bad pixels and columns were removed by interpolating between adjacent pixels and lastly, the individual dithered frames were median combined to remove cosmic ray hits. Calibration was performed using standard stars from Thuan & Gunn (1976). These were used to correct for atmospheric extinction from varying airmass and provide the instrumental zero point. Photometric uncertainties, estimated using these standards, are no more than ≈ 0.05 mag.

Sources in the reduced optical frames were extracted using the DAOPHOT package in IRAF (Stetson 1987). This package has the benefit of performing photometry in crowded fields, which is the case in most regions of our optical fields. It performed the following steps: first, sources were extracted above a given threshold, given as a multiple of the total CCD noise (sky and read noise, σ_{tot}). We adopted threshold values of 4.5-5σ_{tot}, just high enough to avoid large numbers of spurious detections. Second, simple aperture photometry was performed on these identified sources. This required a specification of the aperture radius which is likely to contain most of the light of our target source, and width of a surrounding annulus to estimate and subtract the sky background. We adopted a radius of six arcsec and annulus width of four arcsec. Next, a point spread function (PSF) was determined in each of our nine fields. This involved an interative technique to remove contamination from neighbouring sources in crowded fields near our PSF candidates. Simultaneous PSF fitting on all sources was then performed to identify sources which were previously hidden in crowded regions. Finally, the magnitudes determined from PSF fits were aperture corrected to a common aperture size as used on our standard stars. Aperture corrections were typically 0.22 mag. A final visual inspection removed any spurious detections. A total of $\approx$ 300-390 sources were extracted from each $9.7 \times 9.7\,\mathrm{arcmin}^2$ field to a limit of $r \simeq 25$ mag. Previous optical surveys find typically 380-520 sources within this area to this limit, and the variation is primarily due to clustering. Such fluctuations are found to be significant on

such relatively small scales (eg. Metcalfe et al. 1991).

3.2. Astrometry

The astrometry on the optical images was based on 10-12 APM catlog stars in each field (Maddox et al. 1990). The `ccmap` and `cctran` tasks in the `IRAF immcoords` package were used to compute plate solutions relating pixel positions to astrometric coordinates. Astrometric coordinates for all sources on the frames were then determined. By comparing the positions of several sources common to the APM catalog and our fields, we found that our rms position uncertanties are typically $\lesssim 0.9''$.

4. OPTICAL/NEAR-INFRARED IDENTIFICATION OF RADIO SOURCES

4.1. Method for Optical Identification

We assigned optical identifications and estimate their reliability using a robust likelihood ratio (LR) analysis. This general method has frequently been used to assess identification probabilities for radio and infrared sources (eg. de Ruiter, Willis & Arp 1977; Prestage & Peacock 1983; Sutherland & Saunders 1992; Lonsdale et al. 1998). The method, which computes the probability that a suggested identification is the 'true' optical counterpart, is outlined as follows:

For each optical candidate i in the search area of some radio source j, we calculated the value of the dimensionless difference in radio and optical positions:

$$r_{ij} = \left[\frac{(\alpha_i - \alpha_j)^2}{\sigma_{\alpha_i}^2 + \sigma_{\alpha_j}^2} + \frac{(\delta_i - \delta_j)^2}{\sigma_{\delta_i}^2 + \sigma_{\delta_j}^2} \right]^{1/2}, \quad (1)$$

where the α's and δ's represent right ascensions and declinations respectively, and σ's

standard deviations. We chose a moderately large search radius of $10''$ to allow for the maximal position uncertainties: $\sigma_{\rm opt} \approx 1.4''$ and $\sigma_{\rm rad} \approx 1.5''$ (assuming $5\sigma_{eff}$, where $\sigma_{eff} = (\sigma^2_{\rm opt} + \sigma^2_{\rm rad})^{1/2}$). Such a radius is also small enough to avoid large numbers of chance associations.

Given r_{ij}, we must now distinguish between two mutually exclusive possibilities: (1) the candidate is a confusing background object that happens to lie at distance r_{ij} from the radio source or (2) the candidate is the 'true' identification that appears at distance r_{ij} owing solely to radio and optical position uncertainties. We assume that the radio and optical positions would coincide if these uncertainties were zero. This assumption however is not valid when the centroid of an extended radio source is used, and is further discussed below.

To distinguish between these cases, we compute the likelihood ratio LR_{ij}, defined as:

$$LR_{ij} = \frac{\exp\left[-r^2_{ij}/2\right]}{2\pi N(< m_i)\left[(\sigma^2_{\alpha_i} + \sigma^2_{\alpha_j})(\sigma^2_{\delta_i} + \sigma^2_{\delta_j})\right]^{1/2}}, \qquad (2)$$

where $N(< m_i)$ is the *local* surface density of objects brighter than candidate i. The likelihood ratio LR_{ij} is simply the ratio of the probability of an identification (the Rayleigh distribution: $r\exp(-r^2/2)$), to that of a chance association at r $(2\pi N(< m_i)\sigma_\alpha\sigma_\delta)$. LR_{ij} therefore represents a 'relative weight' for each match ij, and our aim is to find an optimum cutoff LR_c above which a source is taken to be a reliable and likely candidate. Its advantage over alternative methods (purely based on finding the lowest random chance match, eg. Downes et al. 1986) is that it allows for a possible distant candidate to still be the 'true' identification even when there is still a high chance of it being a spurious background source.

It is important to note that our form for LR_{ij} (eq. 2) slightly differs from that used by earlier studies (eg. Lonsdale et al. 1998) in that it doesn't contain the multiplicative

"Q" factor in the numerator. This factor represents the apriori probability that a "true" optical counterpart brighter than the flux limit exists amongst the identifications. For our purposes, we will treat LR_{ij} as simply a a relative weight measure for each radio-optical match, just for the purposes of assigning an optimal cutoff for reliable identification (see below). We are not concerned with its absolute value, which is required when computing formal probability measures from LR. For simplicity, we have therefore set $Q = 1$ in this work.

The optical surface density as a function of magnitude to be used in computing LR was determined from the total number of objects visible in our optical frames. The variation in surface density in the vicinity of each radio source caused by possible clustering effects was found to be small: no more than 5% on $2 - 3'$ scales.

The distribution of LR values for all possible radio source-candidate matches is shown by the shaded histogram in Figure 5. Following Lonsdale et al. (1998), we generate a truly random background population with respect to the radio sources by offseting the radio source positions by $\approx 30''$. LR values for each radio source were then re-computed and their distribution is given by the thick-lined histogram in Figure 5. A comparison of the number of associations for (true) radio source positions with the number of associations found for random (offset) positions will enable us to determine a critical value LR_c for reliable identification. From these distributions, we compute the reliability as a function of LR:

$$R(LR_{ij}) = 1 - \frac{N_{random}(LR_{ij})}{N_{true}(LR_{ij})}, \tag{3}$$

where N_{true} and N_{random} are the number of true and random associations respectively. The reliability computed in this way also represents an approximate measure of the identification probability for a candidate with given LR.

Figure 6 illustrates the reliability as a function of LR. Above $\log(LR) \sim 0.5$, the reliabilities are $\gtrsim 85\%$ because few random associations exceed this value of LR (Fig. 5). As

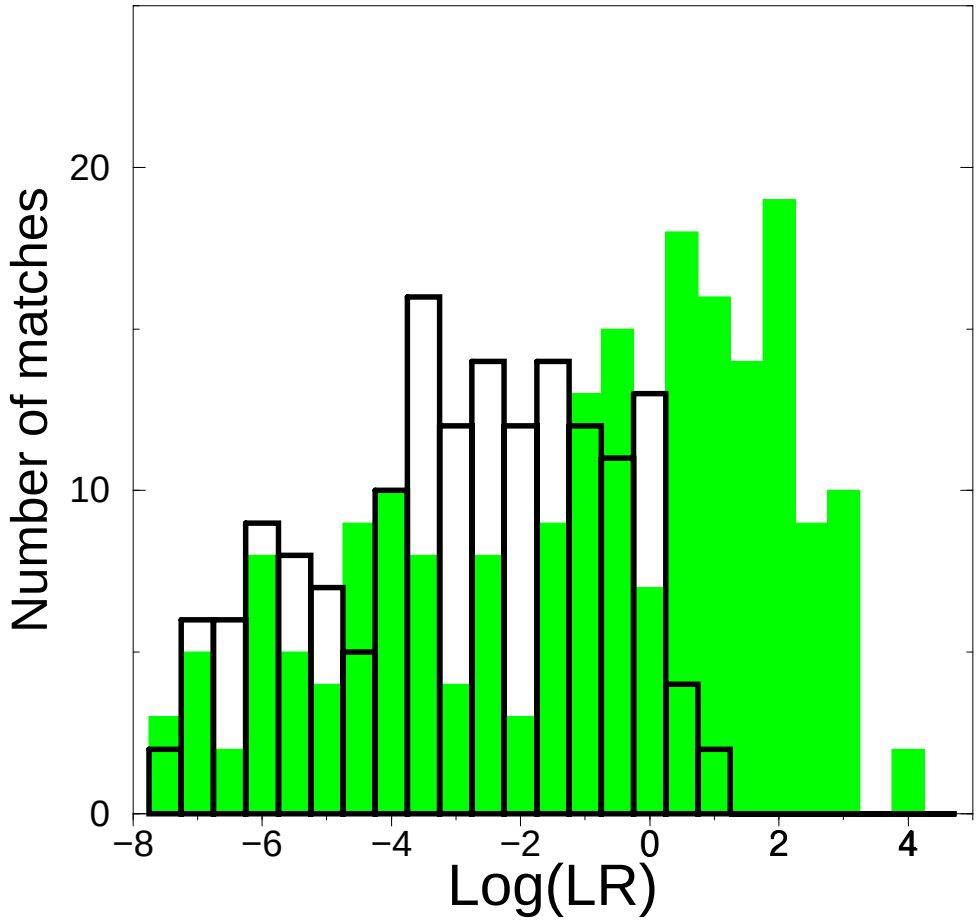

Fig. 5.— Distribution of LR for radio-optical matches at "true" radio positions (shaded histogram), and at "random" radio positions (thick-lined histogram).

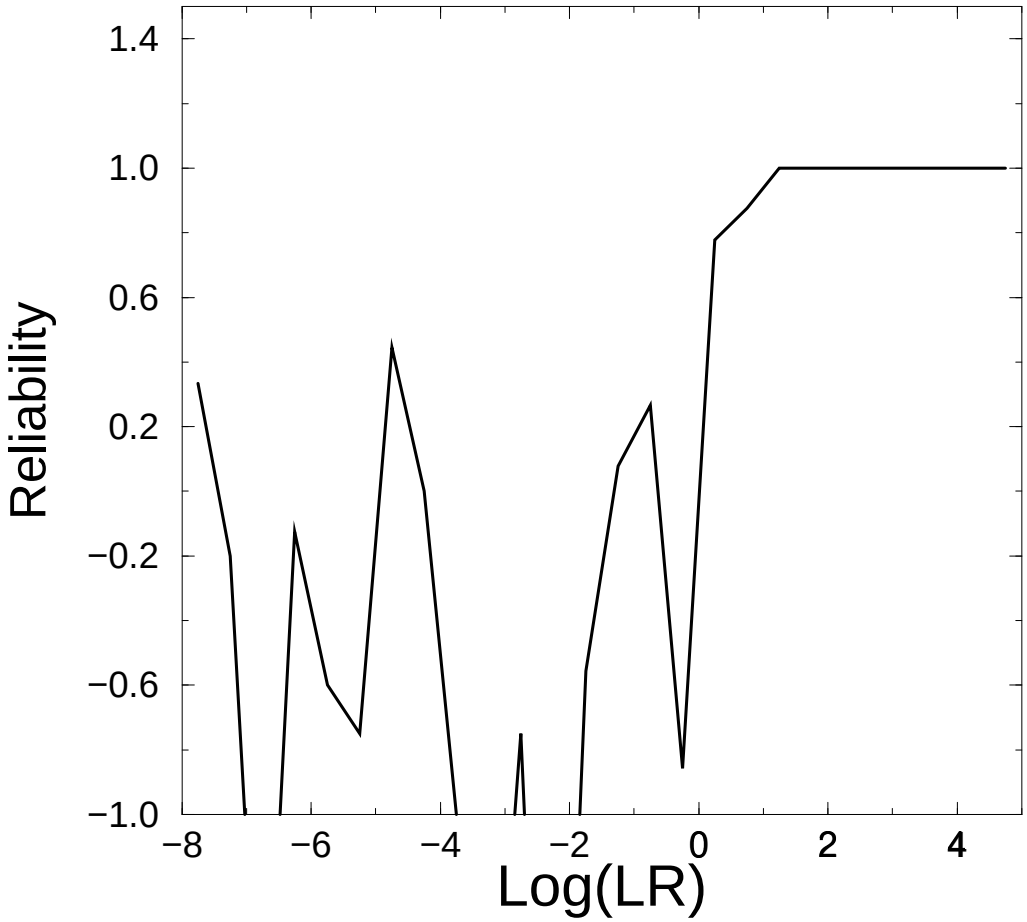

Fig. 6.— Reliability as a function of LR. See equation (3).

a good working measure we therefore assume a cutoff $\log(LR_c) \simeq 0.5$ above which a source is taken to be a likely candidate. The determination of reliabilities via the LR method is insensitive to variations in $N(< m_i)$ across the field or uncertainties in its derivation, and also the assumption of Gaussian error ellipses in the radio and optical positions. Such uncertainties are "normalised out" when one computes the ratio of random to true number of associations within a search radius when estimating the reliability (eq. 3). Lonsdale et al. (1998) have shown that the absolute value of LR itself depends on the characteristics of the source population being identified (eg. stars versus galaxies). Different populations (assuming they could be classified a-priori using some diagnostic) map into different underlying surface densities at the 'identifying' wavelength, implying that distributions in LR (eq. 2) will also be different. For a robust determination of the reliability in such situations, see Lonsdale et al. (1998).

There are two complications to consider in the above method. The first is when one attempts to identify extended (or resolved) radio sources with this method. For all radio sources, we have used the positions of centroids derived from two-dimensional Gaussian fits in computing the LR for optical candidates. For unresolved sources with (Gaussian fitted) sizes $\lesssim 15''$ (the synthesised FWHP beam width), the source is likely to have a compact central component and the optical position is expected to lie close to its quoted radio centroid. For an extended (resolved) source however, the radio and optical positions may differ considerably since errors in the radio centroids are only $\lesssim 2''$. In such cases, if $LR < LR_c$ the identification may still be valid, since its low LR value could purely be due to a real large positional offset. The second complication is when a radio source has more than one optical candidate within its search radius with $LR > LR_c$. This occured in about 20% of cases and was primarily due to contaminating stars. We assess these ambiguities and increase the robustness of our identifications by visually examining all optical candidates according to the following criteria:

1. If candidates have $LR < LR_c$ for a radio source with $\theta_{min,max} \gtrsim 15''$, then identification is classified as *uncertain*.

2. If candidates have *very low* reliability, $LR \ll LR_c$ (for *unresolved* radio sources), or there are no objects in the search radius, then radio source is classified as *empty field*.

3. If $LR \lesssim LR_c$, i.e. where reliability is *moderately "low"*, then identification is also uncertain.

4. If more than one optical candidate exists with $LR > LR_c$, then only source(s) with extended (galaxy-like) optical profile is taken as the identification. Point sources associated with quasar nuclei are not considered in our identification scheme due to their relatively low surface density compared to galaxies ($\approx 1:4000$) in sub-millijansky radio samples.

5. For unique, $LR > LR_c$ candidates, its optical profile is also checked for confirmation.

4.2. Results

Of the 62 radio sources, 43 lie within our optically imaged $27.5 \times 27.5\,\mathrm{arcmin}^2$ field. We found optical identifications for 26 to $r \simeq 25$ mag with reliabilities $R_{id} \gtrsim 80\%$. Four sources have identifications classified as uncertain owing to a moderately low identification reliability of $R_{id} \lesssim 78\%$ (and $\log(LR) \lesssim 0.4$). Five more are uncertain because they have extended radio structure and large possible positional offsets between optical and radio centroid positions. Eight radio sources lie in "definite" optical empty fields with no candidates brighter than $r \simeq 25$ mag.

Other optical follow-up studies found similar results. Georgakakis et al. (1999) identified $\approx 47\%$ of sources to $R = 22.5$ mag from the Phoenix Deep Survey ($S_{1.4\mathrm{GHz}} > 0.2$

mJy) (Hopkins et al. 1998). Deeper indentifications of sources as faint as $S_{1.4\mathrm{GHz}} \simeq 40\mu$Jy from Hubble Deep Field images revealed a 80% success rate to $I = 25$ mag (Richards et al. 1999). Ignoring the uncertain identifications in our study (from criteria 1 and 3 above and which are excluded from our analysis), we find that ≈18% of our sources are unidentified to $r \sim 25$. Accounting for differences in bandpasses and sensitivity, this is broadly consistent with the above studies. Figure 7 shows the distribution of apparent magnitude r for all reliable (robust) and uncertain identifications in our sample.

4.3. Near-Infrared Data

Near-infrared data in the $J(1.25\mu\mathrm{m})$, $H(1.65\mu\mathrm{m})$ and $K_s(2.17\mu\mathrm{m})$ photometric bandpasses were obtained from the Two Micron All Sky Survey (*2MASS*) project database. For multi-band detection of point sources, this survey is currently scanning the sky to sensitivities 16.5, 16.0 and 15.5 mag at signal-to-noise ratios ≈ 7, ≈ 5 and ≈ 7 respectively in J, H and K_s. The data relevant to this study are not yet released in the public catalogs, and was retrieved from the 'internal working database' at *IPAC*[6]. Photometry in this database was determined using custom PSF-fitting software and algorithms are described in Cutri et al. (2000). Since such data have not been subjected to the rigorous quality assurance as that in the public release catalogs, we have examined individual images for quality and any possible systematic uncertainties in the photometry.

To maximise the possible number of detections, we searched for near-infrared counterparts to each radio source with a conservatively low signal-to-noise ratio threshold of ~ 5 in each band. In cases where a source was detected in only one or two of the three bandpasses: J, H and K_s, we note its "band-filled" 95% confidence upper-limit in

[6]The Infrared Processing and Analysis Center, California Institute of Technology.

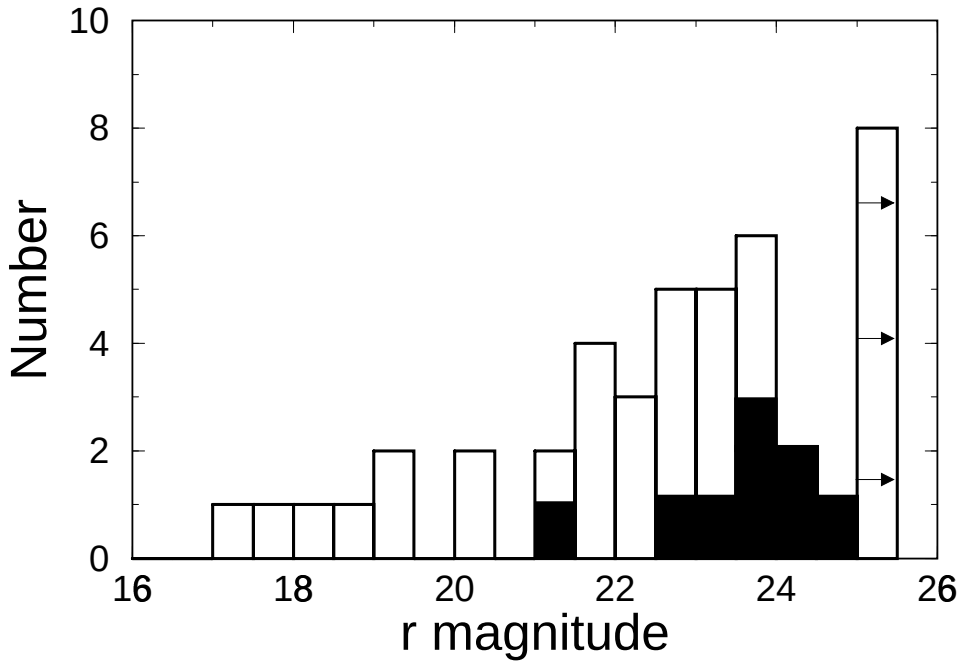

Fig. 7.— The distribution of apparent r-band magnitudes for the 26 identified radio sources (open histogram) and nine uncertain identifications (filled histogram). Eight empty fields are represented by the $r > 25$ magnitude bin with arrows.

the undetected band. In other words, the *2MASS* catalog also reports upper limits to measurements in an undetected band by placing an aperture over the position inferred from detections in other bands. The image pixel scale of the *2MASS* detectors is 2.0″ and the positional uncertainties are $\lesssim 0.5''$. Owing to the relatively shallow flux limits of the *2MASS* survey, the background source surface density is low enough that chance associations with radio positions are very unlikely.

We searched the *2MASS* database for near-infrared counterparts to our 43 radio sources that have *available optical* information from our deep optical survey and examined their images for quality. We found 7 reliable matches with 6 detections in J, 7 in H, and 4 in K_s at the $\gtrsim 5\sigma$ level. Upper limits were available for the remainding "band-filled" values.

Results of our optical identification analysis and available near-infrared data are shown in Table 3. In column order, this table reports: the radio source name (see Table 2); RA and Dec.(J2000) of the optical counterpart of the radio source; optical-radio position separation ($\delta_{rad-opt}$) in arcsec; logarithm of the liklihood ratio (LR); reliability of the optical identification (see eq.[3]); apparent r-band magnitude; J, H and K_s magnitudes with errors or 2σ upper limits; $r-H$ color; $r-K_s$ color, and last, the optical morphology if the optical counterpart is visually resolved with size $\gtrsim 5\theta_{FWHM}(PSF)$.

Optical morphologies were determined from light profile fitting of individual sources and comparison with $R^{1/4}$-law (elliptical-like) and exponential (disk-like) profiles. In cases where a disturbed or interacting morphology is apparent, then it is designated to have an irregular (labelled as 'Irr') morphology. Sources unresolved in the optical with typically $\lesssim 5\theta_{FWHM}(PSF)$ are designated as 'unknown' and labelled as '?' in Table 2.

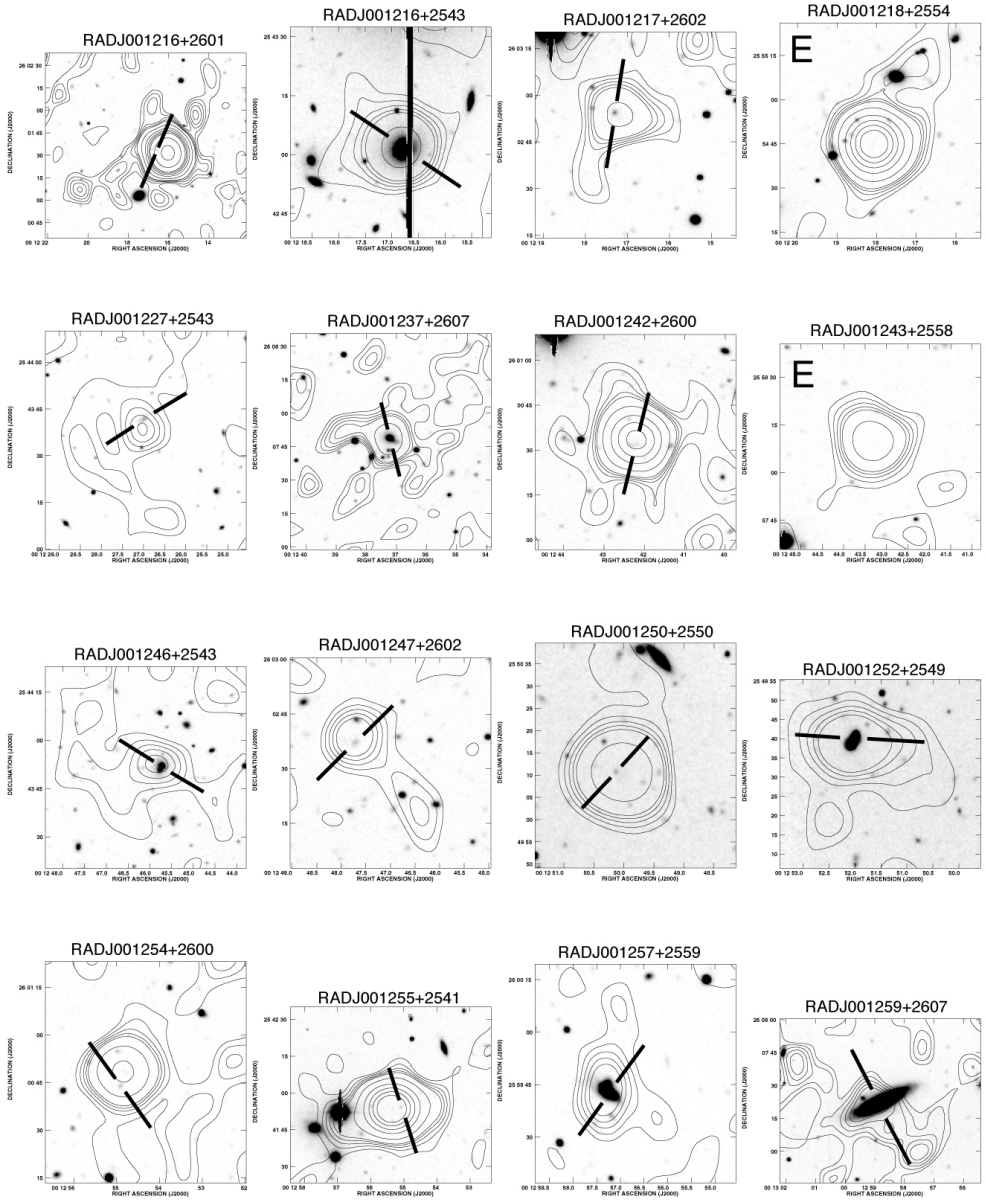

Fig. 8.— Optical image (r-band) and radio contour overlays for the 43 sources with available optical information. Contour levels are 1σ, 2σ, 3σ, 4σ, 5σ, 10σ, 20σ, 30σ, 40σ, 50σ, 100σ and 200σ, where σ refers to the local rms noise (see Table 1). Optical candidates are indicated within broken lines—see Table 3 for reliability estimates. Maps labelled with "E" in upper left corner represent optical empty fields.

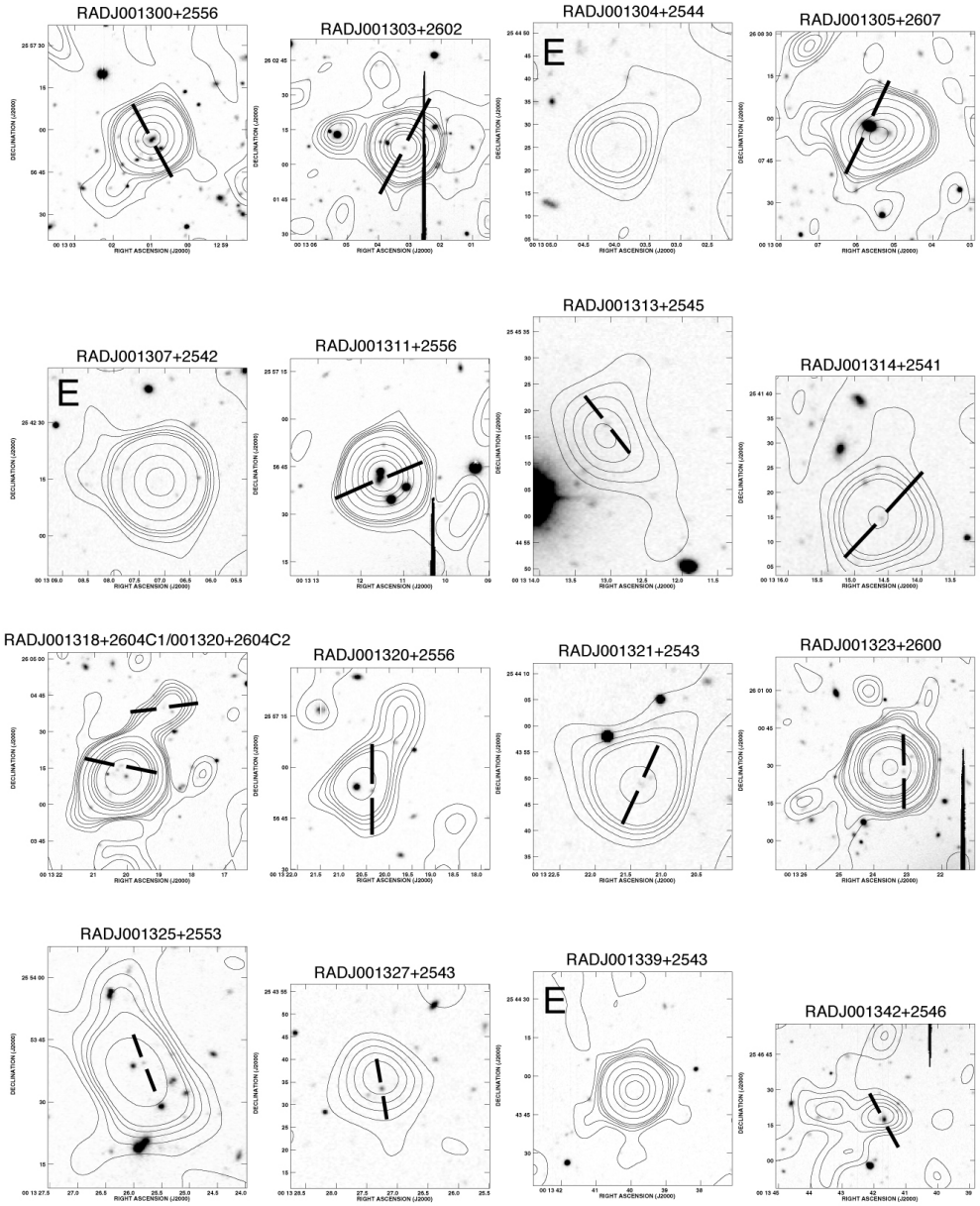
RADJ001300+2556
RADJ001303+2602
RADJ001304+2544
E
RADJ001305+2607
RADJ001307+2542
E
RADJ001311+2556
RADJ001313+2545
RADJ001314+2541
RADJ001318+2604C1/001320+2604C2
RADJ001320+2556
RADJ001321+2543
RADJ001323+2600
RADJ001325+2553
RADJ001327+2543
RADJ001339+2543
E
RADJ001342+2546

Fig. 8.— contd...

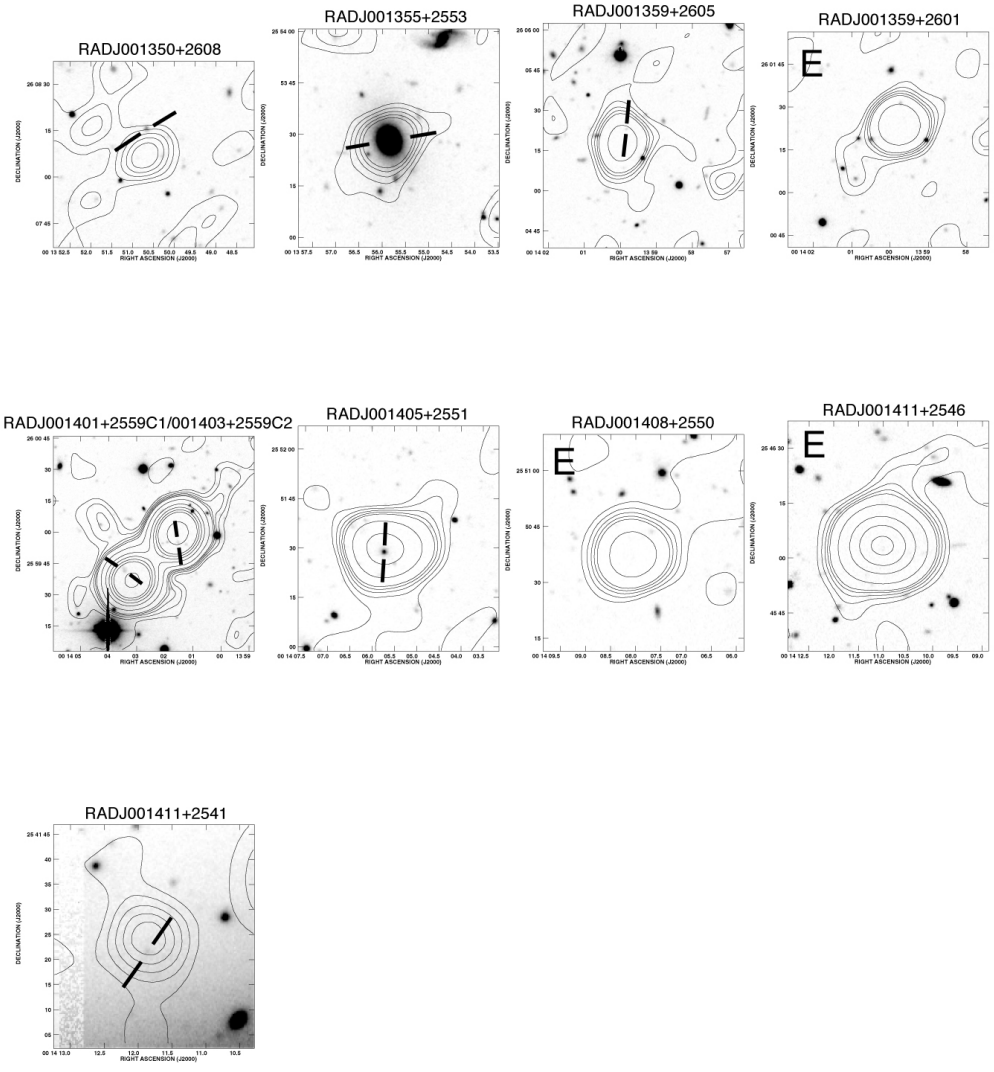
RADJ001350+2608
RADJ001355+2553
RADJ001359+2605
RADJ001359+2601
E
RADJ001401+2559C1/001403+2559C2
RADJ001405+2551
RADJ001408+2550
E
RADJ001411+2546
E
RADJ001411+2541
DECLINATION (J2000)
RIGHT ASCENSION (J2000)

Fig. 8.— contd...

4.4. Optical and Radio Map Overlays

In Figure 8 we show the optical image – radio map overlays for the 43 radio sources with available optical information. A visual inspection of the optical images of resolved counterparts shows a diverse morphological mix, consistent with previous studies. About 40% of our optical identifications have elliptical/disk-like morphology, while $\sim$ 10% can be identified as exhibiting peculiar (either interacting or disturbed) morphologies. It is important to note that these 'disturbed' sources are based on visual inspection alone and their morphology could still be uncertain until future spectroscopy confirms their nature. The elliptical/disk hosts also tend to be associated on average with sources of relatively brighter radio flux density ($\gtrsim$ 2 mJy) than the irregular class. This is consistent with previous radio-optical identification studies which find an increasing fraction of irregular-type galaxies at $S_{1.4} \lesssim 2$ mJy (eg. Kron, Koo, & Windhorst 1985, Hammer et al. 1995, Gruppioni et al. 1998) and a significant number of elliptical galaxies hosting the brighter extended radio galaxies and AGN (Condon 1989).

A further observation is the unique radio structure exhibited by our eight optical empty field sources with $r > 25$ mag. These are represented by maps in Fig. 8 labelled by the letter "E". All show compact and symmetric (presumably unresolved) structures and could represent either of the following: distant (possibly dusty) AGN where with our radio sensitivity, we could have detected a nominal FR-I galaxy to $z \sim 1.3$, or, nearby, compact dusty starbursts at $z \lesssim 0.3$ as constrained by typical starburst luminosities: $L_{1.4\mathrm{GHz}} \lesssim 10^{23}\mathrm{W\,Hz^{-1}}$. The second explanation for the nature of the empty fields is more plausible, given that the majority of submillijansky radio sources are associated with star-forming galaxies and less than 5% are usually identified with bright FR-Is at $z \lesssim 1$ (Kron, Koo & Windhorst 1985).

EDITOR: PLACE FIGURE 8 HERE.

5. ANALYSIS OF RADIO AND OPTICAL–NEAR-INFRARED COLORS

This section presents an analysis of flux ratios between the radio, near-infrared, and optical bands to explore possible contributions from AGN and starbursts to the observed radio emission as well as the importance of absorption by dust. Because we lack spectroscopic information, our analysis treats the sub-mJy sources as one homogeneous population and uses a simple stellar synthesis model to interpret its properties quantitatively.

5.1. A Simple Synthesis Model

We can predict the radio–to–optical(–near-IR) flux ratios and $r - K$ colors for a range of galaxy types using the stellar population synthesis code of Bruzual & Charlot (1993) (hereafter BC). On its own however, the BC model does not directly predict the amount of radio emission expected from a star-forming galaxy, which we need for the determination of flux ratios involving the radio band. We do this by relating the star-formation rates derived from empirical calibrations involving the UV and radio bands as follows.

The 1.4 GHz radio emission from star-forming systems is believed to be primarily synchrotron emission from cosmic rays accelerated in supernova remnants plus a small ($\sim 10\%$) thermal contribution from HII regions (Condon & Yin 1990, Condon 1992). Thus to a good approximation, the radio luminosity is taken to be proportional to the formation rate of stars with $M > 5M_{\odot}$:

$$SFR(M \geq 5M_{\odot}) = \frac{L_{1.4\mathrm{GHz}}}{4 \times 10^{28} \mathrm{erg\ s^{-1}Hz^{-1}}} M_{\odot}\mathrm{yr}^{-1}. \quad (4)$$

(Condon 1992). These same massive stars will also contribute significantly to the UV continuum emission in the range $\sim$ 1200-2500Å. In particular, there have been many different calibrations of the SFR from the UV-flux. For a Salpeter initial mass function (IMF) from $mM_{\odot}$ to $100M_{\odot}$, the calibration of Madau et al. (1998) (which assumes *no*

dust correction) yields

$$SFR(M \geq mM_{\odot}) = Q_m \left(\frac{L_{UV}}{7.14 \times 10^{27} \mathrm{erg\ s^{-1} Hz^{-1}}} \right) M_{\odot} \mathrm{yr}^{-1}. \quad (5)$$

We have modified the initial relation of Madau et al. (1998) to include the factor Q_m, which represents the fraction of stellar masses contributing to the observed SFR,

$$Q_m = \frac{\int_{mM_{\odot}}^{100M_{\odot}} M\psi(M)dM}{\int_{0.1M_{\odot}}^{100M_{\odot}} M\psi(M)dM}, \quad (6)$$

where $\psi(M) \propto M^{-x}$ is the IMF. For $m = 0.1$, we have $Q_m = 1$. Assuming a Salpeter IMF ($x = 2.35$), we find that for stars with $M > 5M_{\odot}$, $Q_m \simeq 0.18$. With this fraction, and equating the two SFR calibrations (eqs [4] and [5]), we find that the luminosity densities at 1.4 GHz ($L_{1.4GHz}$) and $\simeq 2100$Å (L_{UV}) are very nearly equal. We therefore assume that the rest frame 1.4 GHz flux density is directly given by the flux density at $\simeq 2100$Å as specified by the synthesized model spectrum. In general terms, the observed radio flux (in the same units as the synthesised UV spectrum) can be written:

$$f_{\nu}(1.4\mathrm{GHz})_{obs} = (1+z)^{1-\alpha} f_{\nu}(2100\text{Å})_{rest}, \quad (7)$$

where $\alpha \simeq 0.8$ is the radio spectral index (Condon 1992) and $f_{\nu}(2100\text{Å})_{rest}$ is the rest frame (unreddened) UV spectral flux. We must emphasise that this relative radio flux is only that associated with the star-formation process. Possible additional contributions, such as contaminating AGN, are not considered in this model.

We calculated flux ratios involving the radio, near-infrared and optical bands using evolutionary synthesis models for ellipticals (E/SO), early (Sab/Sbc) and late (Scd/Sdm) type spirals, and "very blue" starbursts (SB). These are meant to represent the possible contributions to the sub-mJy radio sources, and each class is defined by a characteristic star formation rate as a function of time. As supported by local observations (eg. Gavazzi & Scodeggio 1996), we assumed that E/SO and Sab/Sbc galaxies have an exponentially

decaying SFR of the form $\psi(t) \propto \tau^{-1} \exp(-t/\tau)$, where τ is the e-folding time. Values of $\tau = 1$ and $\tau = 8$ Gyr were adopted for the E/SO and Sab/Sbc galaxies respectively. For late-type spirals (Scd/Sdm) and young starbursts (SB), we assumed constant SFRs with different ages. All models used to generate the spectral energy distributions (SEDs) are summarised in Table 4. The models assume $H_0 = 50\,\mathrm{km\,s^{-1}\,Mpc^{-1}}$, $q_0 = 0.5$ and a galaxy formation redshift $z_f = 10$, which corresponds to an age of 12.7 Gyr at $z = 0$.

To explore the effects of dust on our flux ratios and colors, each model SED was reddened in the source rest frame with an extinction curve $\xi(\lambda) \equiv A_\lambda / A_V$ characteristic of the Small Magellanic Cloud (SMC), which appears to be a good approximation for the ISM of nearby galaxies (Calzetti et al. 1994). This approximation is most accurate for the reddest wavelengths of starburst galaxy spectra (7000Å-3μm), although breaks down severely at $\lambda \lesssim 2500$Å(Calzetti et al. 1999). We have used the analytical fit for $\xi(\lambda)$ as derived by Pei (1992) for the SMC. For simplicity, we assumed that the dust is distributed in a homogeneous foreground screen at the source redshift.

5.2. Data and Model Comparions

In Figure 9 we plot the radio–to–optical flux ratio, $R(1.4/r)$, defined as

$$R(1.4/r) = \log(S_{1.4}/\mathrm{mJy}) + 0.4\,r, \tag{8}$$

where $S_{1.4}$ and r are the radio flux and optical r-band magnitude respectively. The distribution seen in observed values of $R(1.4/r)$ is larger at the faintest optical magnitudes $r > 21.5$. There are few galaxies however with $r < 21.5$, and nonetheless, the scatter at $r > 21.5$ is consistent with that found at $r \lesssim 19$ in a larger follow-up study of sub-mJy radio sources by Georgakakis et al. (1999).

Figure 10 shows $R(1.4/r)$ as a function of $r - H$ color for all sources with available

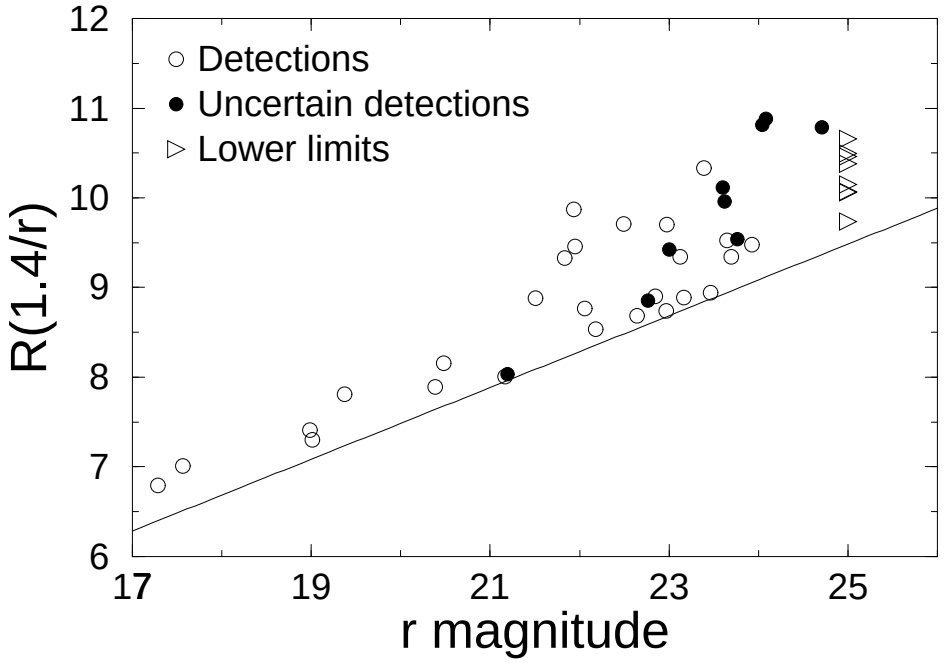

Fig. 9.— Radio–to–optical (r-band) flux ratio (see eq.[8]) as a function of r magnitude for all radio sources with available optical information. For the observed range of r-magnitudes, the solid line represents the prediction at the limiting flux of the survey $S_{1.4\mathrm{GHz}} \approx 0.3$ mJy.

optical and near-infrared data. Our reason for using $r - H$ color is that the H band yielded more "definite" detections than the other near-infrared bandpasses. Although the numbers are still relatively small, this facilitates the best comparison with the synthesis models. The predictions for four galaxy types (see Table 4 and §5.1) are shown for no dust reddening (thin curves) and a rest-frame extinction $A_V = 2.5$ mag. The morphological mix of data shows a relatively large dispersion in $r - H$ color that is more consistent with the range predicted by the models that *include dust*. This suggests that on average, the optical–to–near-infrared continua of most sources in Fig. 10 are reddened by a uniform (possibly "optically thin") dust component with $A_V \simeq 2 - 2.5$ mag absorption. This measure is consistent with spectroscopic studies of nearby starbursts by Calzetti et al. (1996), Meurer et al. (1997) and photometric modelling by Nakata et al. (1999).

We must emphasise that our models only account for radio emission produced from star-formation processes. The sources labelled as elliptical (or early type) in Fig. 10 are not expected to lie on any of the star-formation derived locii. An AGN most likely dominates their radio emission. We include them here merely as a comparision, and their relationship to normal starbursts is discussed further below.

The sources in Fig. 10 appear more-or-less consistent with the dusty "0.1 Gyr starburst" model. This could in principle apply to the two sources with spiral/disk-like morphology (labelled "S"), but is unconventional for the five elliptical morphologies (see below). A comparison with radio–to–near-infrared flux ratios further constrains the underlying properties of these sources. Figure 11 shows the radio–to–near-infrared flux ratio $R(1.4/H)$, defined analagous to eq.[8], as a function of $r - H$ color. The near-infrared emission is dominated by old stars and is less affected by dust than the optical. The radio–to–near-infrared flux ratio should therefore be relatively insensitive to dust. Given the simplicity of our models, the two disk-like sources may not necessarily represent "0.1

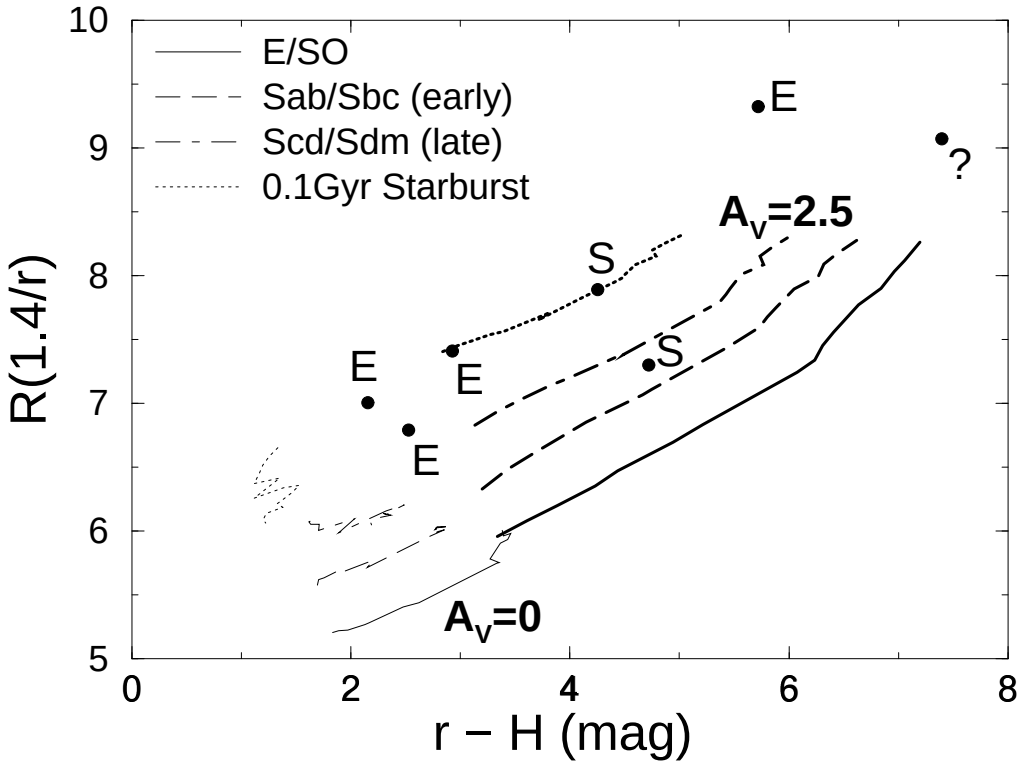

Fig. 10.— Radio–to–optical (r-band) flux ratio (see eq.[8]) as a function of $r - H$ color for radio sources with available optical and near-infrared detections. The predictions of four synthesis models for $0 \leq z \leq 1.5$ ($z = 0$–starting bottom left of curves to $z = 1.5$–top right) are also shown. These assume no extinction (thin curves) and with a rest-frame extinction $A_V = 2.5$ mag (thick curves).

Gyr starbursts" as indicated in Fig. 11. They could also belong to the Sab/Sbc or Scd/Sdm classes. For this to be true, the following additional components may play an important role in more 'realistic' models: 'optically-thick' dust that *completely obscures* both the H and r emission without causing appreciable reddening in $r - H$ color, or, contamination by at least an order of magnitude times more radio emission from a central AGN than that produced purely by supernovae. The second possibility is favored by radio observations of a number of luminous infrared galaxies by Norris et al. (1988), where some showed evidence for significant radio emission from compact Seyfert-like nuclei.

The large discrepancy between the four sources with elliptical morphologies (labelled "E") and predictions from the early-type E/SO models suggests the importance of a significant AGN contribution to the radio emission. Appreciable amounts of optically-thick dust suppressing the optical and near-infrared light (except for extinction by diffuse, optically-thin dust) is not favored by observations (eg. Goudfrooij & de Jong 1995). Most, if not all of these ellipticals are likely to be radio-powered by AGN. At the limiting sensitivity of our radio survey ($\simeq 0.3$ mJy), a nominal FR-I galaxy (with $L_{1.4} = 10^{24}\,\mathrm{WHz}^{-1}$) could be detected to $z \simeq 1.3$, and indeed the spread in $r - H$ color for the ellipticals in Fig. 11 is consistent with the E/SO (optically-thin dust) model to this redshift. A comparison between the model $R(1.4/H)$ values with actual observed values implies that such AGN will contribute a factor 10^2 times more radio emission than that produced by any underlying star formation activity in these systems. It is important to note that the ratio of AGN-to-stellar powered radio activity has a huge spread for the elliptical population in general, and that the factor 10^2 only illustrates a property specific to the ellipticals in our radio sample.

To summarise, our use of a simple synthesis model that includes radio emission and dust reddening to analyse the properties of sub-mJy radio sources has shown the following: first, the presence of dust with extinctions $A_V \simeq 2$ mag and possibly greater, consistent

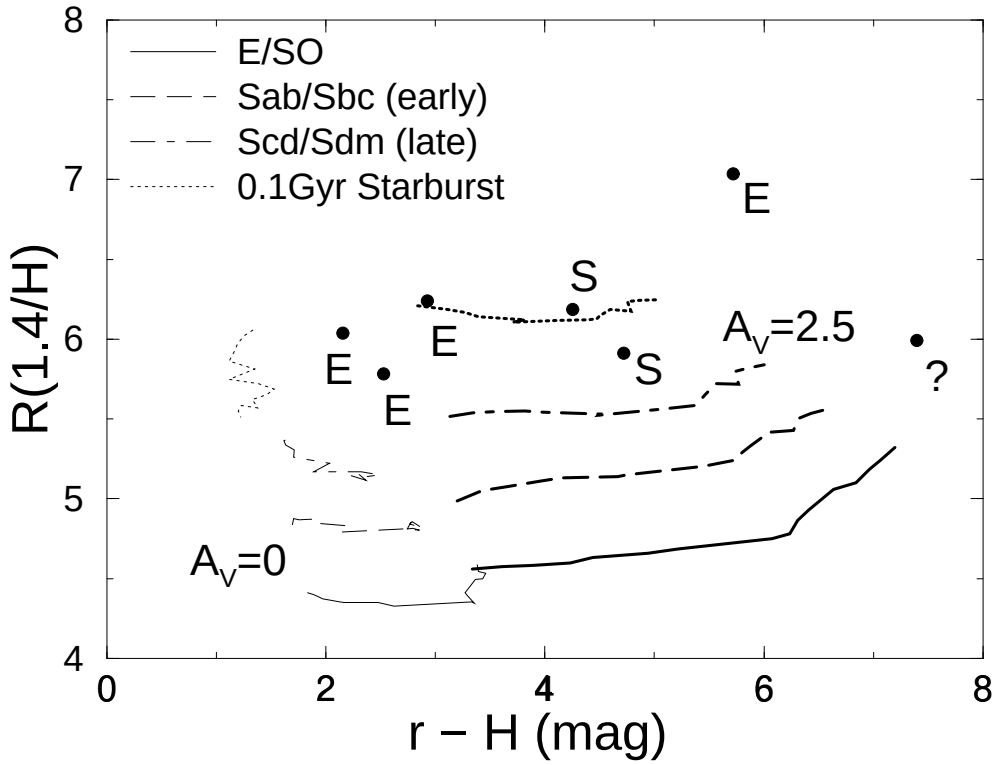

Fig. 11.— Radio–to–near-infrared (H-band) flux ratio as a function of $r - H$ color and models which include no extinction (thin curves) and $A_V = 2.5$ mag (thick curves).

with previous more direct determinations, and second, that the level of radio emission from non-stellar processes such as AGN could be easily inferred and constrained. This will be particularly important for starbursts hosting Seyfert nuclei where a comparison with more sophisticated dust models may be required to infer the relative contributions.

6. A Method to Select "ULIGS" via Radio/Optical Color

Since the emission (and dust absorption) properties from normal galaxy populations are reasonably well known, a color-color diagram such as Fig. 10 could provide a potential diagnostic for selecting ultraluminous infrared galaxies (ULIGS) to high redshift. The relatively low sensitivity of the Infrared-Astronomical Satellite (IRAS) has primarily confined ULIG selection to the local Universe (Sanders & Mirabel 1996), although there is some speculation that recently discovered faint "SCUBA" sources at sub-millimetre wavelengths could represent their high-redshift counterparts (eg. Blain et al. 1999). Approximately 80% of local ULIGS are believed to be powered by starbursts and the remainder show evidence for an AGN contribution (Genzel et al. 1998; Lutz et al. 1998). Far-infrared observations have shown that dust and molecular gas in local ULIGS is concentrated in compact regions $\lesssim$ 1kpc (Okumura et al. 1991, Bryant 1996) and that a large fraction of the optical/UV emission is hidden by optically-thick dust (Sanders et al. 1988). A study of their properties and importance to galaxy evolution therefore requires observations at wavelengths virtually immune to dust absorption. Radio frequencies provide an excellent window of opportunity.

Figure 12 illustrates the predicted locus in color-color space using the synthetic SEDs of three local far-IR selected systems: Arp 220 ($L_{IR} \simeq 1.6 \times 10^{12} L_{\odot}$) - a ULIG undergoing a powerful starburst as seen via high resolution radio observations by Smith et al. (1998); M82 ($L_{IR} \simeq 6 \times 10^{10} L_{\odot}$) - a system undergoing a weak-to-moderate starburst, and Mrk

273 ($L_{IR} \simeq 2.6 \times 10^{12} L_{\odot}$) - a ULIG whose bolometric emission is believed to be dominated by a hidden central AGN from the presence of strong Seyfert-2 lines and moderately strong hard X-ray (2-10 keV) emission (Turner et al. 1997). We have used the synthetic SEDs generated by Devriendt et al. (1999) to model the starburst emission. These authors used a self-consistent modelling approach to predict the stellar optical/UV/near-IR emission, its reprocessing into the mid-IR–to–sub-mm by dust, and the nonthermal stellar-powered radio emission based on the empirical radio–to–far-IR luminosity correlation. Due to its strong AGN-dominated nature, the starburst synthetic SED predicted by Devriendt et al. for Mrk 273 differs appreciably from that observed in the *radio*. For this source, we therefore used the Devriendt et al. SED at wavelengths $\lambda < 1$mm and extrapolated into the radio using its actual *observed* radio–to–1mm spectral slope and fluxes (obtained from the NASA/IPAC Extragalactic Database [7]).

Figure 12 shows that a galaxy characteristic of the (low-IR luminous) M82 system will occupy a region similar to that occupied by normal galaxies in this study (and also their predicted synthetic colors in Fig. 10). Luminous systems classified as ULIGS however (Arp 220 and Mrk 273), will tend have higher radio–to–optical flux ratios which could be easily selected. This can be explained by the well-observed correlation between far-infrared luminosity and far-IR ($60 - 100\mu$m)–to–optical spectral slope (Soifer et al. 1987). Consequently, the most IR-luminous systems with the largest far-IR–to–optical ratios are also likely to have a high level of radio-emission due to its strong correlation with IR luminosity. This will lead to a larger than average radio–to–optical flux ratio for ULIGS in general as shown in Fig. 12.

---

[7]The NASA/IPAC Extragalactic Database (NED) is operated by the Jet Propulsion Laboratory, California Institute of Technology, under contract with the National Aeronautics and Space Administration.

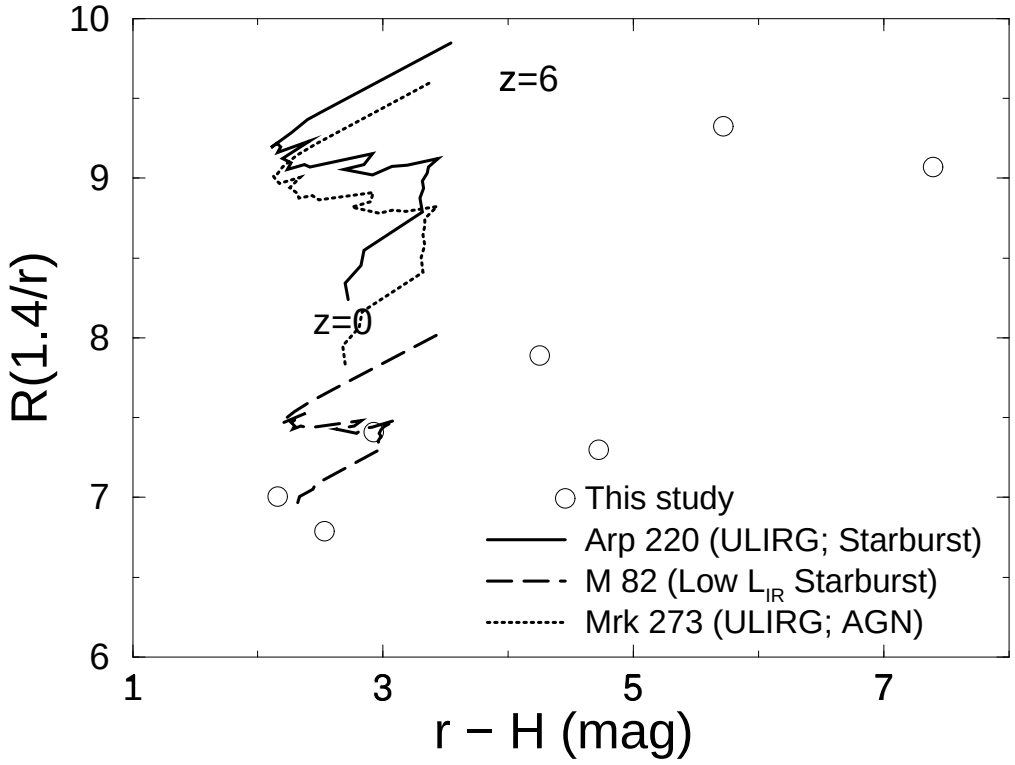

Fig. 12.— Locus of observed radio–to–optical flux ratio versus $r - H$ color for $0 \leq z \leq 6$ ($\Delta z = 0.2$) using three local far-IR selected systems: Arp 220 ($L_{IR} \simeq 1.6 \times 10^{12} L_{\odot}$; strong starburst), M82 ($L_{IR} \simeq 6 \times 10^{10} L_{\odot}$; weak/moderate starburst) and Mrk 273 ($L_{IR} \simeq 2.6 \times 10^{12} L_{\odot}$; AGN dominated).

The existence of systems with either larger rest-frame optical/UV extinction or excess AGN contribution to the radio than the ULIGS considered here will be shifted further upwards on this plot. Diagnostics to distinguish between AGN and starburst dominated ULIGS using radio-to-optical color alone will not be trivial and is left to a future study. The three ULIGS in Fig. 12 represent a range of known ULIGS and their location on this plot simply serves as a diagnostic to pre-select ULIG candidates for further study.

A system like Arp 220 (with $\nu L_\nu(1.4\mathrm{GHz}) \simeq 2.5 \times 10^6 L_\odot$) could be observed to redshift $z \sim 1.6$[8] if initially selected from a radio survey limited to $S_{1.4\mathrm{GHz}} \simeq 50\mu$Jy. Thus, to limiting sensitivities reached by existing 1.4 GHz surveys, such a method may not probe the highest redshifts. Nonetheless, as shown in Fig. 12, such systems could still be well separated from normal galaxies to this redshift. Assuming an Arp 220-like SED and moderate luminosity evolution ($L_{60\mu\mathrm{m}} \propto (1+z)^{2.5}$), the surface density of ULIGS to $z \sim 1.6$ is expected to be of order $150\,\mathrm{deg}^{-2}$ at $S_{1.4\mathrm{GHz}} \gtrsim 50\mu$Jy, or about 6% of the integral count to this sensitivity (Richards 2000). They should therefore exist in significant numbers in deep large-area radio surveys.

7. SUMMARY AND CONCLUSIONS

We have used the VLA radio telescope to image a contiguous $33 \times 33\,\mathrm{arcmin}^2$ area to a (mean) limiting (5σ) sensitivity of $\simeq 0.35$ mJy. From a total of 62 detections, the results of optical and near-infrared photometry are reported for 43 sources. Our optical photometry is more sensitive than previous optical follow-up studies of radio surveys of similar depth. Our main findings are:

(1) We have used a robust, likelihood-ratio method for determining optical

[8]Assumes $q_0 = 0.5$, $H_0 = 50\,\mathrm{km\,s^{-1}\,Mpc^{-1}}$

identifications and their reliability. This method is seldom used in identification studies and is insensitive to assumptions concerning fluctuations in background source density and Gaussian error distributions. We assigned optical candidates to 26 radio sources with reliability $\gtrsim 80\%$. Nine radio sources are uncertain and/or ambiguous, and eight are empty fields. Near-infrared photometry from the *2MASS* database was reported for 7 sources.

(2) The eight optical empty field sources all display compact and symmetric radio morphologies and most probably represent compact starbursts at $z \lesssim 0.3$ strongly obscured by dust. They may require at least 4 magnitudes optical extinction to account for their large radio–to–optical flux ratio compared to the identified population. Our conclusion for them being 'compact starbursts' is very tentative as it is purely based on starburst versus AGN number statistics expected from sub-mJy radio surveys. Further deep infrared/optical imaging and spectroscopy will be necessary.

(3) Consistent with previous studies, our deep ($r \simeq 25$) optical imaging shows that the optical appearence can be divided into two classes according to radio flux-density: elliptical-like morphologies for $\gtrsim 2$ mJy, and peculiar or disturbed for $\lesssim 2$ mJy.

(4) Using a stellar synthesis model which includes radio emission and dust reddening, we find that the near-infrared–to–optical emission in a small, bright sub-sample is reddened by 'optically thin' dust with $A_V \simeq 2 - 2.5$ mag, regardless of morphological type. This appears consistent with other more direct determinations. Consistent with previous studies, the radio emission from early-type systems seems to be powered by AGN rather than star-formation to account for their anomalously large radio–to–optical(–near-infrared) ratios.

(5) Our analysis shows that a radio/optical or radio/near-IR color selection technique could provide a potential means for detecting ULIG-type objects to $z \sim 1.6$.

Despite the lack of spectroscopic information, our study of a homogeneous population of faint radio sources has stressed the importance of dust on studies of intrinsic galaxy properties and their evolution at optical wavelengths. A future goal would be to obtain spectra, or multi-color optical/near-infrared photometry to better explore these sources and the validity of the simple stellar synthesis models presented in this paper. The ever improving resolution (and sensitivity) capabilities of optical/near-IR detectors over those feasible at (the longest) radio wavelengths requires robust identification techniques to better ascertain their properties. Likelihood-ratios provide one such technique. The present study complements other deep optical studies of faint radio sources to constitute a statistically significant sample for inferring their nature and importance to galaxy evolution.

FJM thanks Glenn Morrison and JoAnn O'Linger for valuable assistance with the data reduction and Rosalie Ewald for assistance with radio/optical image overlays. We thank the staff at Palomar Observatory for technical assistance during the observing run. This publication makes use of data products from the Two Micron All Sky Survey, which is a joint project of the University of Massachusetts and the Infrared Processing and Analysis Center/California Institute of Technology, funded by the National Aeronautics and Space Administration and the National Science Foundation. The National Radio Astronomy Observatory is operated by Associated Universities, Inc., under cooperative agreement with the National Science Foundation. This research has made use of the NASA/IPAC extragalactic database (NED) which is operated by the jet propulsion laboratory, caltech, under contract with the national aeronautics and space administration. FJM acknowledges support from a JPL/NASA postdoctoral fellowship grant.

Table 1. The regions used for the source extractions

Region	RA(J2000)[a]	Dec(J2000)[a]	σ_{rms} (mJy)	5σ limit (mJy)	# sources[b]
1	$00^h13^m48^s.43$	$+25°48'07''.7$	0.061	0.305	15
2	$00^h12^m34^s.09$	$+25°47'11''.7$	0.065	0.325	15
3	$00^h12^m33^s.11$	$+26°03'27''.7$	0.090	0.450	20
4	$00^h13^m48^s.21$	$+26°02'47''.7$	0.076	0.380	14[c]

[a]Defines the center of each region with size $\approx 16.5 \times 16.5\,\mathrm{arcmin}^2$.

[b]Total number of sources with flux density $\geq 5\sigma_{rms}$.

[c]Includes the separate components of two double-component sources.

TABLE 2

Catalog of Radio Source Data

Name	RA(J2000) (h,m,s)	Dec(J2000) (° ′ ″)	σ_{RA} (″)	σ_{Dec} (″)	S_P (mJy)	σ_{S_P} (mJy)	S_T (mJy)	σ_{S_T} (mJy)	θ_M (″)	θ_m (″)	PA (deg)	σ_{θ_M} (″)	σ_{θ_m} (″)	σ_{PA} (deg)
RADJ001158+2550	00 11 58.058	+25 50 24.41	0.37	0.43	1.468	0.095	1.410	0.088	15.944	13.579	169	1.027	0.875	16
RADJ001158+2556	00 11 58.078	+25 56 48.20	0.24	0.26	2.176	0.095	2.820	0.075	14.482	12.969	24	0.630	0.564	16
RADJ001203+2544	00 12 03.977	+25 44 54.18	1.35	1.06	0.424	0.084	0.284	0.116	15.249	9.908	63	3.402	2.210	20
RADJ001204+2540	00 12 04.313	+25 40 37.21	0.22	0.21	2.653	0.092	2.930	0.118	15.797	13.559	51	0.563	0.484	9
RADJ001204+2605	00 12 04.572	+26 05 01.42	0.66	0.61	0.973	0.084	0.962	0.036	18.466	12.055	129	1.795	1.172	9
RADJ001206+2611	00 12 06.178	+26 11 05.20	0.49	0.59	1.096	0.095	1.050	0.046	16.439	13.115	19	1.419	1.132	15
RADJ001209+2540	00 12 09.614	+25 40 24.41	0.30	0.31	1.880	0.093	2.780	0.099	14.993	14.237	29	0.755	0.717	39
RADJ001210+2551	00 12 10.381	+25 51 36.54	0.40	0.43	1.402	0.094	1.300	0.110	16.091	12.989	147	1.086	0.876	13
RADJ001216+2601	00 12 16.041	+26 01 31.64	0.03	0.03	17.676	0.064	18.42	0.108	17.051	15.245	10	0.091	0.081	2
RADJ001216+2543	00 12 16.854	+25 43 02.09	0.60	0.57	0.955	0.084	0.836	0.140	14.521	13.550	100	1.437	1.341	58
RADJ001217+2602	00 12 17.177	+26 02 53.96	0.73	0.61	0.878	0.044	0.844	0.159	16.079	13.462	99	1.732	1.450	24
RADJ001218+2554	00 12 18.056	+25 54 44.99	0.13	0.13	4.580	0.095	4.700	0.173	15.301	15.081	47	0.316	0.311	18
RADJ001218+2539	00 12 18.193	+25 39 42.82	0.07	0.07	8.443	0.095	8.380	0.167	14.927	14.783	16	0.167	0.166	17
RADJ001227+2543	00 12 27.184	+25 43 39.10	3.09	3.67	0.240	0.090	0.408	0.207	26.143	14.623	144	9.884	5.529	25
RADJ001230+2610	00 12 30.123	+26 10 40.53	1.38	1.35	0.734	0.098	1.141	0.201	33.900	13.072	134	4.253	1.640	5
RADJ001237+2607	00 12 37.254	+26 07 48.87	0.54	0.53	1.157	0.089	1.230	0.147	16.823	14.221	49	1.375	1.163	20
RADJ001240+2609	00 12 40.394	+26 09 57.71	1.18	1.57	0.447	0.094	0.419	0.157	18.876	11.192	153	3.994	2.368	16
RADJ001241+2610	00 12 41.007	+26 10 31.16	0.31	0.28	2.006	0.071	1.970	0.116	16.611	13.268	121	0.783	0.626	8
RADJ001242+2600	00 12 42.209	+26 00 33.55	0.18	0.18	3.229	0.095	4.160	0.086	15.278	14.392	62	0.448	0.422	20
RADJ001243+2558	00 12 43.323	+25 58 10.05	0.51	0.50	1.158	0.095	1.130	0.136	15.394	14.207	52	1.257	1.160	41
RADJ001246+2543	00 12 46.030	+25 43 51.08	2.24	1.63	0.344	0.093	0.410	0.123	19.944	13.441	107	5.430	3.659	17
RADJ001247+2602	00 12 47.680	+26 02 38.49	0.86	0.90	0.559	0.094	0.377	0.127	12.744	11.914	21	2.155	2.014	12
RADJ001250+2550	00 12 50.036	+25 50 10.68	0.45	0.46	1.224	0.095	1.050	0.151	14.153	13.629	26	1.094	1.054	83
RADJ001252+2549	00 12 52.006	+25 49 38.49	1.21	0.88	0.655	0.033	0.855	0.130	20.303	14.466	82	2.881	2.053	17
RADJ001254+2600	00 12 54.835	+26 00 48.52	0.34	0.34	1.656	0.095	1.490	0.125	14.504	13.978	130	0.829	0.799	63
RADJ001255+2541	00 12 55.365	+25 41 53.48	0.14	0.12	4.717	0.094	5.470	0.182	17.566	14.852	96	0.351	0.296	5
RADJ001257+2559	00 12 57.288	+25 59 43.59	0.84	1.33	0.544	0.093	0.553	0.155	18.083	11.514	179	3.141	2.000	15
RADJ001259+2607	00 12 59.107	+26 07 18.91	1.86	1.44	0.497	0.089	0.501	0.218	24.476	18.828	84	4.406	3.390	27
RADJ001300+2556	00 13 00.983	+25 56 57.10	0.18	0.18	3.230	0.095	4.070	0.096	15.100	14.147	129	0.442	0.414	18
RADJ001303+2602	00 13 03.185	+26 02 07.41	0.11	0.11	5.136	0.095	5.270	0.097	15.289	15.108	112	0.282	0.278	23
RADJ001304+2544	00 13 04.017	+25 44 25.38	0.89	0.96	0.545	0.094	0.977	0.129	13.924	11.175	146	2.416	1.939	32
RADJ001305+2607	00 13 05.397	+26 07 54.15	0.18	0.16	3.906	0.093	4.990	0.119	19.377	14.842	115	0.462	0.354	4
RADJ001307+2542	00 13 07.094	+25 42 14.25	0.25	0.25	2.384	0.095	3.380	0.091	15.068	14.900	7	0.598	0.591	13
RADJ001311+2556	00 13 11.484	+25 56 41.98	0.12	0.12	4.782	0.095	4.900	0.076	14.915	14.203	150	0.295	0.281	16
RADJ001313+2545	00 13 13.019	+25 45 15.15	1.57	1.75	0.358	0.094	0.529	0.155	17.375	11.916	36	4.588	3.147	28
RADJ001314+2541	00 13 14.646	+25 41 14.85	0.74	0.80	0.723	0.074	0.824	0.121	14.606	13.296	162	1.909	1.738	16
RADJ001318+2604C1	00 13 18.834	+26 04 38.76	1.28	1.09	0.578	0.093	0.597	0.156	22.405	9.339	128	3.666	1.528	7
RADJ001320+2604C2	00 13 20.122	+26 04 11.43	0.05	0.05	12.512	0.092	13.44	0.081	17.148	14.930	130	0.129	0.113	2
RADJ001320+2556	00 13 20.552	+25 56 55.59	0.58	0.71	0.911	0.094	0.993	0.154	17.319	11.884	151	1.797	1.233	11

TABLE 2—*Continued*

Name	RA(J2000) (h,m,s)	Dec(J2000) (° ′ ″)	σ_{RA} (″)	σ_{Dec} (″)	S_P (mJy)	σ_{S_P} (mJy)	S_T (mJy)	σ_{S_T} (mJy)	θ_M (″)	θ_m (″)	PA (deg)	σ_{θ_M} (″)	σ_{θ_m} (″)	σ_{PA} (deg)
RADJ001321+2543	00 13 21.405	+25 43 49.37	0.69	0.70	0.800	0.096	0.888	0.148	14.764	13.115	140	1.745	1.551	10
RADJ001323+2600	00 13 23.522	+26 00 29.25	0.03	0.03	15.877	0.095	16.24	0.097	15.258	15.080	130	0.091	0.090	21
RADJ001325+2553	00 13 25.931	+25 53 37.18	0.56	0.70	1.170	0.092	1.700	0.210	22.747	14.340	30	1.791	1.129	7
RADJ001327+2543	00 13 27.289	+25 43 35.07	1.29	1.22	0.424	0.094	0.332	0.119	13.870	12.706	64	3.091	2.832	13
RADJ001339+2543	00 13 39.899	+25 43 54.55	0.18	0.18	3.140	0.065	4.010	0.161	14.983	14.384	141	0.451	0.433	30
RADJ001342+2546	00 13 42.203	+25 46 18.76	2.95	1.55	0.361	0.030	0.654	0.237	27.823	14.628	92	6.953	3.656	15
RADJ001349+2539	00 13 49.176	+25 39 20.08	0.42	0.35	1.519	0.035	1.450	0.162	16.018	13.413	88	0.998	0.835	14
RADJ001349+2609	00 13 49.935	+26 09 25.19	0.10	0.10	6.301	0.094	7.330	0.088	17.944	14.591	46	0.268	0.218	3
RADJ001350+2608	00 13 50.742	+26 08 06.93	1.31	1.04	0.460	0.094	0.364	0.110	15.341	11.627	107	3.153	2.390	30
RADJ001355+2540	00 13 55.638	+25 40 48.82	1.12	1.15	0.538	0.094	0.547	0.165	16.771	13.643	138	2.945	2.396	34
RADJ001355+2553	00 13 55.874	+25 53 27.52	0.73	0.72	0.760	0.097	1.432	0.135	15.362	12.182	133	1.912	1.516	22
RADJ001359+2601	00 13 59.764	+26 01 23.68	0.41	0.39	1.413	0.095	1.360	0.045	15.092	13.286	124	1.011	0.890	21
RADJ001359+2605	00 13 59.945	+26 05 17.72	0.49	0.63	1.080	0.095	1.090	0.087	17.033	13.351	175	1.492	1.169	14
RADJ001401+2559C1	00 14 01.544	+25 59 59.45	0.06	0.07	9.410	0.094	9.860	0.132	17.264	15.048	150	0.173	0.151	3
RADJ001401+2610	00 14 01.825	+26 10 59.96	1.14	1.04	0.465	0.084	0.329	0.120	13.499	11.792	114	2.742	2.395	31
RADJ001403+2559C2	00 14 03.162	+25 59 37.11	0.08	0.08	8.005	0.088	9.080	0.028	16.501	15.463	140	0.195	0.182	7
RADJ001405+2551	00 14 05.675	+25 51 29.74	0.37	0.30	1.884	0.095	2.100	0.081	17.524	14.319	90	0.879	0.719	10
RADJ001408+2550	00 14 08.057	+25 50 37.67	0.50	0.47	1.172	0.035	1.650	0.072	14.896	13.522	113	1.202	1.091	24
RADJ001410+2610	00 14 10.909	+26 10 35.97	0.32	0.30	1.828	0.095	1.870	0.094	15.161	13.586	60	0.785	0.703	19
RADJ001411+2546	00 14 11.017	+25 46 03.46	0.23	0.20	2.919	0.095	3.190	0.110	16.703	14.714	93	0.541	0.477	10
RADJ001411+2541	00 14 11.856	+25 41 24.11	1.19	1.40	0.417	0.088	0.331	0.140	14.811	12.073	19	3.356	2.736	45
RADJ001416+2610	00 14 16.812	+26 10 51.50	0.86	0.94	0.681	0.093	0.696	0.126	16.754	13.742	149	2.327	1.909	28
RADJ001418+2540	00 14 18.769	+25 40 08.27	0.49	0.54	1.107	0.095	1.200	0.110	15.381	13.182	150	1.314	1.126	12

TABLE 3

Optical-Infrared Data

Name	RA(J2000)[a] (h,m,s)	Dec(J2000)[a] (° ′ ″)	$\delta_{rad-opt}$ (″)	log(LR)	R_{id}[e]	r	J (σ_J)[b]	H (σ_H)	K (σ_K)	$r-H$	$r-K$	morph[c]
RADJ001216+2601[d]	00 12 16.530	+26 01 32.77	7.41	-4.163	$\ll 0.1$	24.083(?)	...	...	...	...	...	?
RADJ001216+2543	00 12 16.783	+25 43 01.34	1.31	3.537	≈ 1	17.565	16.056(0.093)	15.409(0.138)	14.525(0.086)	2.156	3.040	E
RADJ001217+2602	00 12 17.280	+26 02 54.85	1.78	1.514	≈ 1	22.057	...	...	...	...	...	E
RADJ001218+2554	...	...	...	...	...	>25	...	...	...	...	...	...
RADJ001227+2543	00 12 27.033	+25 43 41.19	3.09	0.685	0.862	22.971	...	...	...	...	...	Irr
RADJ001237+2607	00 12 37.248	+26 07 48.49	0.39	2.883	≈ 1	19.371	...	...	...	...	...	S
RADJ001242+2600[d]	00 12 42.347	+26 00 30.83	3.42	0.278	0.783	23.621(?)	...	...	...	...	...	?
RADJ001243+2558	...	...	...	...	...	>25	...	...	...	...	...	?
RADJ001246+2543	00 12 45.777	+25 43 50.59	3.83	1.293	≈ 1	21.169	...	...	...	...	...	E
RADJ001247+2602[d]	00 12 47.889	+26 02 35.96	4.03	0.302	0.788	22.768(?)	...	...	...	...	...	E
RADJ001250+2550	00 12 50.137	+25 50 10.86	1.52	1.225	0.995	23.128	...	...	...	...	...	E
RADJ001252+2549	00 12 51.969	+25 49 38.81	0.65	2.919	≈ 1	18.984	17.416(0.285)	16.057(0.204)	>16.321	2.927	<2.663	E
RADJ001254+2600[d]	00 12 54.855	+26 00 44.70	3.83	0.246	0.764	23.004(?)	...	...	...	...	...	?
RADJ001255+2541[d]	00 12 55.064	+25 41 54.13	4.56	-0.689	$\ll 0.1$	23.599(?)	...	...	...	...	...	?
RADJ001257+2559	00 12 57.287	+25 59 43.60	0.03	2.248	≈ 1	20.384	17.066(0.210)	16.131(0.225)	>15.178	4.253	<5.206	S
RADJ001259+2607	00 12 59.187	+26 07 19.09	1.21	2.706	≈ 1	19.010	15.158(0.074)	14.290(0.075)	13.913(0.074)	4.720	5.097	S
RADJ001300+2556	00 13 01.007	+25 56 57.08	0.35	1.505	≈ 1	22.974	...	...	...	...	...	Irr
RADJ001303+2602	00 13 03.204	+26 02 07.27	0.31	1.681	≈ 1	22.492	...	...	...	...	...	E
RADJ001304+2544	...	...	...	...	...	>25	...	...	...	...	...	?
RADJ001305+2607	00 13 05.293	+26 07 53.81	1.60	1.675	≈ 1	21.835	>16.403	16.118(0.207)	>14.996	5.717	<6.839	E
RADJ001307+2542	...	...	...	...	...	>25	...	...	...	...	...	...
RADJ001311+2556	00 13 11.603	+25 56 41.19	1.95	1.515	≈ 1	21.950	...	...	...	...	...	Irr
RADJ001313+2545	00 13 13.049	+25 45 17.44	2.33	0.778	0.882	23.464	...	...	...	...	...	?
RADJ001314+2541	00 13 14.595	+25 41 14.73	0.78	1.118	0.967	23.698	...	...	...	...	...	?
RADJ001318+2604C1	00 13 18.794	+26 04 37.24	1.64	1.189	0.984	22.847	...	...	...	...	...	Irr
RADJ001320+2604C2	00 13 20.199	+26 04 10.69	1.37	1.706	≈ 1	21.938	...	...	...	...	...	E
RADJ001320+2556	00 13 20.705	+25 56 53.85	2.88	1.647	≈ 1	20.481	...	...	...	...	...	E
RADJ001321+2543	00 13 21.339	+25 43 48.81	1.15	0.996	0.936	22.929	16.206(0.104)	15.536(0.128)	15.224(0.179)	7.393	7.705	?
RADJ001323+2600[d]	00 13 23.256	+26 00 27.73	4.28	0.247	0.775	24.040(?)	...	...	...	...	...	?
RADJ001325+2553	00 13 25.803	+25 53 39.14	2.75	0.695	0.864	23.650	...	...	...	...	...	?
RADJ001327+2543	00 13 27.260	+25 43 33.55	1.58	1.265	≈ 1	22.639	...	...	...	...	...	E
RADJ001339+2543	...	...	...	...	...	>25	...	...	...	...	...	...
RADJ001342+2546[d]	00 13 41.666	+25 46 16.96	8.27	0.238	0.770	21.194(?)	...	...	...	...	...	Irr
RADJ001350+2608	00 13 50.572	+26 08 12.05	4.73	0.617	0.858	22.178	...	...	...	...	...	E
RADJ001355+2553	00 13 55.857	+25 53 28.22	0.75	3.729	≈ 1	17.286	15.642(0.071)	14.756(0.082)	14.419(0.098)	2.530	2.867	E
RADJ001359+2601	...	...	...	...	...	>25	...	...	...	...	...	...
RADJ001359+2605[d]	00 13 59.795	+26 05 22.01	4.84	-0.760	$\ll 0.1$	23.763(?)	...	...	...	...	...	?
RADJ001401+2559C1	00 14 01.559	+25 59 57.15	2.31	0.861	0.903	23.390	...	...	...	...	...	?
RADJ001403+2559C2[d]	00 14 03.088	+25 59 33.06	4.20	-0.790	$\ll 0.1$	24.707(?)	...	...	...	...	...	?
RADJ001405+2551	00 14 05.728	+25 51 28.88	1.16	1.893	≈ 1	21.508	...	...	...	...	...	E
RADJ001408+2550	...	...	...	...	...	>25	...	...	...	...	...	...
RADJ001411+2546	...	...	...	...	...	>25	...	...	...	...	...	...
RADJ001411+2541	00 14 11.805	+25 41 22.34	1.93	1.016	0.938	23.164	...	...	...	...	...	?

[a] Refers to optical position.
[b] Values with ">" are 2σ upper limits on measured fluxes, otherwise, errors are quoted in parenthesis.
[c] Optical morphology: E—Elliptical, Irr—Irregular or Disturbed, S—Spiral, ?—Unknown.
[d] Optical identification uncertain due to either extended radio emission and large offset from radio centroid position, or, 'moderately low' LR value.
[e] Reliability of the optical identification. Cases with 'very low' and 'very large' $log(LR)$ are listed with $R_{id} \ll 1$ and $R_{id} \approx 1$ respectively.

Table 4. Population synthesis models

Type	SFR(t)	IMF	Age (Gyr)[a]
E/SO	$\tau_1^{-1} \exp(-t/\tau_1)$	Scalo	12.7
Sab/Sbc	$\tau_8^{-1} \exp(-t/\tau_8)$	Scalo	12.7
Scd/Sdm	constant	Salpeter	12.7
SB	constant	Salpeter	0.1

[a]For the SB-type, an age of 0.1 Gyr is assumed to apply at all redshifts. For other types, this refers to the present day age.

REFERENCES

Benn, C. R., Rowan-Robinson, M., McMahon, R. G., Broadhurst, T. J., & Lawrence, A., 1993, MNRAS, 263, 98

Blain, A. W., Smail, I., Ivison, R. J., & Kneib, I. -P., 1999, MNRAS, 302, 632

Bruzual, A. G., & Charlot, S., 1993, ApJ, 405, 538

Bryant, P., 1996, In *CO observations of Luminous Infrared Galaxies*, PhD thesis, California Institute of Technology

Calzetti, D. Kinney, A. L., & Storchi-Bergmann, T., 1994, ApJ, 429, 582

Calzetti, D. Kinney, A. L., & Storchi-Bergmann, T., 1996, ApJ, 458, 132

Calzetti, D., Armus, L., Bohlin, R. C., Kinney, A. L., Koornneef, J., Storchi-Bergmann, T., 2000, ApJ, 533, 682

Ciliegi, P., McMahon, R. G., Miley, G., Gruppioni, C., Rowan-Robinson, M. et al., 1999, MNRAS, 302, 222

Condon, J. J., 1989, ApJ, 338, 13

Condon, J. J., & Yin, Q. F., 1990, ApJ, 357, 97

Condon, J. J., 1992, A&A Rev., 30, 575

Condon, J. J., 1997, PASP, 109, 166

Condon, J. J., Cotton, W. D., Greison, E. W., Yin, Q. F., Perley, R. A., Taylor, G. B., & Broderick, J. J., 1998, AJ, 115, 1693

Cram, L. E., 1998, ApJ, 506, L85

Cram, L. E., Hopkins, A. M., Mobasher, B., & Rowan-Robinson, M., 1998, ApJ, 507, 155

Cutri et al., 2000, Explanatory Supplement to the 2MASS Second Incremental Data Release, http://www.ipac.caltech.edu/2mass/releases/second/doc/explsup.html

Danese, L., De Zotti, G., Franceschini, A., & Toffolatti, L., 1987, ApJ, 318, L15

de Ruiter, H. R., Willis, A. G., & Arp, H. C., 1977, A&AS, 28, 211

Devriendt, J. E., Guiderdoni, B., & Sadat, R., 1999, A&A, 350, 381

Downes, A. J. B., Peacock, J. A., Savage, A., Carrie, D. R., 1986, MNRAS, 218, 31

Fanaroff, B. L., & Riley, J. M., 1974, MNRAS, 167, 31

Gavazzi, G., & Scodeggio, M., 1996, A&A, 312, L29

Georgakakis, A., Mobasher, B., Cram, L., Hopkins, A., & Lidman, C., 1999, MNRAS, 306, 708

Genzel, R., Lutz, D., Sturm, E., Egami, E., Kunze, D., Moorwood, A. F. M., Rigopoulou, D., Spoon, H. W. W., Sternberg, A., Tacconi-Garman, L. E., Tacconi, L., and Thatte, N., 1998, ApJ, 498, 579

Goudfrooij, P., & de Jong, T., 1995, A&A, 298, 784

Gruppioni, C., Mignoli, M., & Zamorani, G., 1998, MNRAS, 304, 199

Haarsma, D. B., Partridge, R. B., Waddington, I., & Windhorst, R. A., 1999, 19th Texas Symposium on Relativistic Astrophysics and Cosmology, Paris 1998, ed. J. Paul, T. Montmerle, & E. Aubourg (CEA Sarclay), 600

Haarsma, D. B., Partridge, R. B., Windhorst, R. A., & Richards, E. A., 2000, astro-ph/0007315, To appear in ApJ

Hammer, F., Crampton, D., Lilly, S. J., Le Fèvre, O., & Kenet, T., 1995, MNRAS, 276, 1085

Helou, G., Soifer, B. T., & Rowan-Robinson, M., 1985, ApJ, 298, L7

Hopkins, A. M., Mobasher, B., Cram, L., & Rowan-Robinson, M., 1998, MNRAS, 296, 839

Kells, W., Dressler, A., Sivaramakrishnan, A., Carr, D., Koch, E., Epps, H., Hilyard, D., & Pardeilhan, G., 1998, PASP, 110, 1487

Kron, R. G., Koo, D. C., & Windhorst, R. A., 1985, A&A, 146, 38

Lonsdale, C. J., Conrow, T., Evans, T., Fullmer, L., Moshir, M., Chester, T., Yentis, D., Wolstencroft, R., MacGillivray, H., & Egret, D., 1998, New Horizons From Multi-Wavelength Sky Surveys, Proc. IAU Colloquium 179, Johns Hopkins University, ed. B. McLean, D. Golombek, J. Hayes, & H. Payne, Kluwer Academic Publishers, p. 450

Lutz, D., Spoon, H. W. W., Rigopoulou, D., Moorwood, A. F. M., Genzel, R., 1998, ApJ, 505, L103

Madau, P., Ferguson, H. C., Dickinson, M. E., Giavalisco, M., Steidel, C. C., & Fruchter A., 1996, MNRAS, 283, 1388

Madau, P., Pozetti, L., Dickinson, M., 1998, ApJ, 498, 106

Maddox, S. J., Sutherland, W. J., Efstathiou, G., Loveday, J., 1990, MNRAS, 243, 692

Metcalfe, N., Shanks, T., Fong, R., Jones, L. R., 1991, ApJ, 249, 498

Meurer, G., Heckman, T. M., Lehnert, M. D., Leitherer, C., & Lowenthal, J., 1997, AJ, 114, 54

Mitchell, K. J. & Condon, J. J., 1985, AJ, 90, 1957

Mobasher, B., Cram, L., Georgakakis, A., & Hopkins, A., 1999, MNRAS, 308, 45

Nakata, F., Shimasaku, K., Doi, M., Kashikawa, N., Kawasaki, W. et al., 1999, MNRAS, 309, L25

Norris, R. P., Allen, D. A., & Roche, P. F., 1988, MNRAS, 234, 773

Okumura, S. K., Kawabe, R., Ishiguro, M., Kasuga, T., Morita, K. I., Ishizuki, S., 1991, In *Dynamics of Galaxies and Their Molecular Cloud Distributions*, ed. F. Combes, F. Casoli, p. 425, Dordrecht:Reidel

Oort, M. J. A., 1987, A&AS, 71, 221

Pei, Y. C., 1992, ApJ, 395, 130

Prestage, R. M., & Peacock, J. A., 1983, MNRAS, 204, 355

Richards, E. A., Fomalont, E. B., Kellermann, K. I., Windhorst, R. A., Partridge, R. B., Cowie, L. L., Barger, A. J., 1999, ApJ, 526, L73

Richards, E. A., 2000, astro-ph/9908313, To appear in ApJ

Rowan-Robinson, M., Benn, C. R., Lawrence, A., McMahon, R. G., & Broadhurst, T. J., 1993, MNRAS, 263, 123

Sanders, D. B., Soifer, B. T., Elias, J. H., Madore, B. F., Matthews, K., Neugebauer, G., Scoville, N. Z., 1988, ApJ, 325, 74

Sanders, D. B., & Mirabel, I. F., 1996, ARA&A, 34, 749

Schaerer, D., 1999, astro-ph/9906014, To appear in Building the Galaxies: from the Primordial Universe to the Present, XIXth Moriond astrophysics meeting, F. Hammer et al. (eds.), Editions Frontieres (Gif-sur-Yvette)

Scoville, N. Z., Sargent, A. I., Sanders, D. B., & Soifer, B. T., 1991, ApJ, 366, L5

Serjeant, S., Gruppioni, C., & Oliver, S., 1998, preprint astro-ph/9808259

Smith, H. E., Lonsdale, C. J., Lonsdale, C. J., & Diamond, P. J., 1998, ApJ, 493, 17

Soifer, B. T., Sanders, D. B., Madore, B. F., Neugebauer, G., Danielson, G. E., Elias, J. H., Lonsdale, C J., & Rice, W. L., 1987, ApJ, 320, 238

Stetson, P. B., 1987, PASP, 99, 191

Sutherland, W., & Saunders, W., 1992, MNRAS, 259, 413

Thuan, X. T., & Gunn, J. E., 1976, PASP, 88, 543

Thuan, X. T., & Condon, J. J., 1987, ApJ, 322, L9.

Thuan, X. T., Windhorst, R. A., Puschell, J. J., Isaacman, B. R., & Owen, F. N., 1984, ApJ, 285, 515

Turner, T. J., George, I. M., Nandra, K., Mushotzky, R. F., 1997, ApJS, 113, 23

Windhorst, R. A., Miley, K. G., Owen, F. N., Kron, R. G., & David, C. K., 1985, ApJ, 289, 494

Windhorst, R. A., Fomalont, E. B., Partridge, R. B., Lowenthal, J. D., 1993, ApJ, 405, 498

This manuscript was prepared with the AAS LaTeX macros v4.0.